






 Bartholomeusz first author 2000-2006 Davies Boutte Yang Frazier ChemChip Xurography Fluidics

View Arrange By Action Share Edit Tags

Name	^	Date Modified	Size	Kind
 Bartholomeusz 2000 Bioluminescence ChemChip IEEE-EMBS France Frazier.pdf		Oct 11, 2006, 5:20 PM	1.9 MB	PDF
 Bartholomeusz 2002 ICBC Photodetector Calibration.pdf		Oct 10, 2006, 9:45 PM	917 KB	PDF
 Bartholomeusz 2004 ISBC Nanoliter Assays ChemChip Davies Yang .pdf		Apr 1, 2006, 9:39 AM	992 KB	PDF
 Bartholomeusz 2005 Xurography Boutte.pdf		Dec 13, 2005, 8:39 PM	2.4 MB	PDF
 Bartholomeusz 2006 Multi-analyte Microfluidics chips Davies SPIE 6080-46 .pdf		Sep 13, 2011, 10:06 AM	1.5 MB	PDF

BIOLUMINESCENT BASED CHEMCHIP FOR POINT-OF-CARE DIAGNOSTICS

Daniel A. Bartholomeusz (1) and Joseph D. Andrade (2)

Lab for the Modeling, Measurement, and Management of the Metabolome (4M Lab), Department of Bioengineering - University of Utah, 50 S. Campus Center Dr. 2480 MEB, Salt Lake City, UT 84112-9202, USA - Tel +1 801 581 4379, Fax ... 585-5361 Email (1) d.bartholomeusz@m.cc.utah.edu, (2) joe.andrade@m.cc.utah.edu

A. Bruno Frazier, Member, IEEE

School of ECE, Georgia Institute of Technology, Atlanta, GA 30332, USA - Tel +1 404 894 2030, Email frazier@ece.gatech.edu

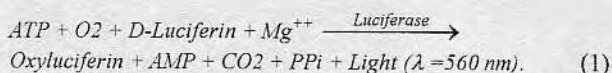
Abstract –The design and progress of a MEMS prototype biochip device, which uses bioluminescence as a means for detecting a potential of 10-100 total analytes from biofluid samples, is discussed. Light enhancement was explored by coating etched square chambers with chromium and silver. Light enhancement was also investigated by observing the transmittance of light along micro channels molded in PDMS. Bioluminescent light generated from a 1-mM ATP with firefly luciferase/luciferin solution was placed inside the channels and chambers and the light output was observed through a close up lens by a CCD. Light enhancement effectiveness was determined from the CCD count increase per nL of sample volume for the cross sectional viewing areas of the channels or chambers. Uncoated silicon, chromium coated and silver coated square chambers enhanced light output about 1-4 CCD counts/ nL, 3-13 CCD counts/nL, and 300 to 1,300 CCD counts/nL respectively. Uncoated PDMS channels enhance light by about 79-101 CCD counts/nL.

I. INTRODUCTION

Current blood work and metabolic analysis in hospitals generally utilize independent and in-house labs. Point-of-Care (POC) devices are able to reduce analysis time, cost, and sample volume by using enzymatic, chromatographic, electrochemical, and immunochromatographic methods. Bioluminescence is a relatively underdeveloped method for metabolic diagnostics in POC devices [1], [2]. It is 100 to 1,000 times more sensitive than conventional measurements and is accurate over five or more orders of magnitude. Therefore, bioluminescence has the sensitivity and range to decrease sample volumes of blood and urine, etc., currently used for *in vitro* diagnostics by at least 100 fold (down to 0.1 to 1.0- μ L or less).

Firefly bioluminescence results from the enzyme-catalyzed oxidation of luciferin utilizing adenosine triphosphate (ATP) [1]. Bacteria bioluminescence is closely coupled to nicotinamide adenine dinucleotide (NADH). Since most of biochemistry depends on ATP and/or NADH, nearly all metabolic reactions can be monitored by coupling

them to an ATP or NADH bioluminescent reaction. The production or consumption of a metabolite of interest causes a change in concentration of ATP (or NADH) through enzyme-linked reactions. The change in light intensity will be stoichiometrically proportional to the dynamic concentration of ATP (or NADH) and thus proportional to the metabolite of interest [1], [2]. Detectable light is produced via the following reaction (for ATP):



Widespread use of bioluminescent-based metabolite detection has been limited due to the instability of the enzymes and the expensive and cumbersome light detection equipment. Recent advances in bioluminescent enzyme preparation has enabled greater enzyme stability and enhanced light output for multi-enzymatic reactions [3], [4]. These procedures have the potential to make the incorporation of bioluminescence into small microfabricated reaction chambers possible. The light output from these microfabricated chambers can then be detected by an inexpensive and hand held CCD-based detection device.

A. Applying MEMS Technology for Miniaturized Bioluminescent Reactions

MEMS can be used to create an array of microfabricated channels or chambers (or ChemChip) for multiple metabolite measurement based on bioluminescence. Through careful design of the micro-fluidics, the channels or chambers can enhance, focus or amplify the light output to decrease the signal to noise ratio while minimizing sample size.

1) *Light integration using the Beer-Lambert Law:* The transmittance of light through a media along a channel or chamber of length ℓ , is defined by the Beer-Lambert Law as $T = 10^{-\text{Absorbance}}$, where $\text{Absorbance} = \epsilon_{\lambda} C_B (\ell - x)$, ϵ_{λ} is the molar absorption coefficient (L/mol·cm) and C_B is the

concentration (mole/L) [5]. If light is generated from within a homogeneous media, the transmitting light is integrated along the length it travels and the total transmittance ($T_{Total(\ell)}$) is defined as:

$$T_{Total(\ell)} = \int_0^{\ell} 10^{-\epsilon C_B (\ell-x)} dx = \frac{(1-10^{-k\ell})}{kLn10} \quad (2)$$

where $k = \epsilon C_B$. Because k will vary as a function of the bioluminescent-based enzyme constituents and their concentrations, we plot $T_{Total(\ell)}$ versus channel length ℓ (Fig. 1) for various values of k and observe the change in expected transmittance of light through a chamber that has length ℓ . For each curve, there is a region where $T_{Total(\ell)}$ increases almost linearly with ℓ . The smaller k is, the longer the linear region before $T_{Total(\ell)}$ plateaus. Therefore, by increasing the length of the channel (or depth of chamber) in which the bioluminescent reaction is occurring, we can increase the intensity of the signal being sent to the detector. This property will be effective up to a certain length (depending on k) and then will become ineffective for the extra sample volume required to fill the longer channels. One method of increasing the effective transmittance length ℓ of a micro-chamber is to coat it with a reflective surface. A reflectance coefficient of 1.0 would essentially double the effective optical path allowing the light to integrate without increasing the volume. Lower reflectance coefficients would not be as effective. We experimented with this by coating chambers, ranging from 50 to 250- μ m deep, with chromium (reflectance = 0.68 at $\lambda = 560$ nm) and with silver (reflectance = 0.86 at $\lambda = 560$ nm). This method will work best for bioluminescent cocktails with a high k value. The other method we experimented with was to simply create long narrow channels ranging from 0.25 to 2.5-cm and compare the light output per sample volume (which is proportional to ℓ).

II. METHODS

1) *Fabrication of shallow micro reaction chambers with light enhancing reflective surface:* Square micro reaction chambers ranging from 10 to 750- μ m were anisotropically etched into nine 3" silicon <100> wafers at 50, 100, and 250- μ m depths. A 30% by weight KOH solution at 82°C etched the <100> plane at 6.32m/hr and produced chambers with a 469.5-Å rms roughness (measured by a Tencor P-10

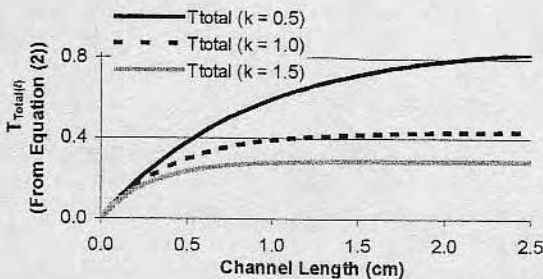


Fig. 1. Total Transmittance of Light from a Homogeneous Light Generating Media Along Various Channel Lengths (ℓ) - At Various Values of k .

profiler). This slow etch rate was used to produce a smooth reflective surface for the experiment. Three silicon wafers were coated with chromium on a 600-Å titanium seed layer (1500-Å, sputtered, reflectance = 0.68 at $\lambda = 560$ nm). Another three wafers were coated with silver (1000-Å, e-beam deposition, reflectance = 0.86 at $\lambda = 560$ nm). The remaining three wafers were left untreated (for silicon, the reflectance ≈ 0 at $\lambda = 560$ nm). The results of the comparison of light output between silicon and chromium was published previously [6]. Here we include silver coated substrates in the comparison.

2) *ChemChips with long narrow channels:* Instead of etching channel into silicon, we decided mold the channels into Poly(dimethylsiloxane) (PDMS -white opaque- RTV E, Dow Corning, Midland, MI) as a method for creating a rapid prototype of our channels. We followed PDMS molding methods reported by Whitesides et al. [7] with minor variations. Various lengths of straight channel arrays (Fig. 2) were patterned into negative photoresist (SU-8 10, Microlithography Chemical Corp., Newton, MA) spin-coated (800-rpm for 40-sec) onto the polished side of unoxidized 4" wafers. After development, the channel thickness was verified at 38.1 ± 0.1 - μ m with a Tencor P-10 Surface Profiler.

The PDMS was prepared in a 10:1 ratio of prepolymer and curing agent according to the manufacturer's instructions. A tiny drop of vacuum oil was smeared on the outer perimeter of the wafer to facilitate removal of the PDMS after molding. The PDMS was poured onto the master (about 5-mm thick) and degassed in a vacuum for 1-minute while on the cast. The cast was then cured at 65°C for 1-hour. The channel arrays were cut out of the PDMS such that the ends of the channels were exposed. These arrays were then placed onto glass slides cleaned with DI water by conformal contact with slight finger pressure, leaving the ends of the channels open at the edge of the glass (Fig. 3). Glass was used to seal the PDMS channels so that the capillarity could be visualized. The PDMS was not oxidized with a plasma cleaner as described by Whitesides et al. [7] so that the PDMS would not stick irreversibly with glass. This allowed the channels to be cleaned and reused during the bioluminescent light measurements.

3) *Light measurements from the shallow micro-chambers with light enhancing reflective surface:* A 1.84- μ M firefly luciferase (Promega)/1.25-mM luciferin (Biosynth) luciferin solution was prepared according to



Fig. 2. ChemChip Straight Channel Array. There are seven sets of channel widths, 250, 200, 150, 100, 75, 50 and 25- μ m, each in sets of 5. Each wafer had two sets of channel arrays for each value of ℓ (25, 20, 15, 10, 7.5, 5.0, 2.5 and 1.5-mm long).

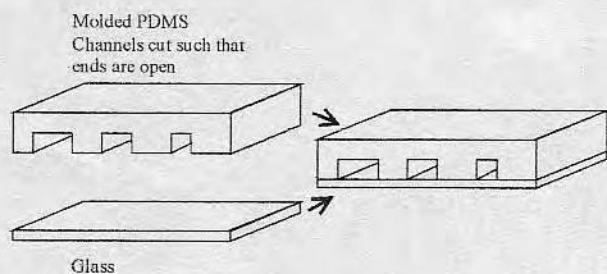


Fig. 3. PDMS Slab Sealing to Top of the V-Channels. Both ends of the sealed channels are open to air. At one end, the bioluminescent fluid is applied. The light is detected "end on" from the other side.

similar methods used in previous research [8], [9]. Other constituents in this solution included 1.25-mg/mL bovine serum albumin (Sigma - used for coating the glass vial to prevent denaturing of the luciferase), 1.25-mM ethylene diaminetetra acetic acid (Sigma), 12.5-mM Mg^{++} (Sigma - from $MgSO_4$), in a 1.25mM glycyl-glycine buffer. This mixture was able to maintain 90% activity for about 10-hours when stored in the dark at room temperature. A 5-mM ATP, glycyl-glycine buffer solution was also prepared. The firefly luciferase/luciferin solution and the ATP solution were mixed in a 20:5 volumetric ratio, resulting in a 1.5- μ M luciferase, 1.0-mM luciferin, and 1.0-mM ATP mixture. This high ratio of ATP to luciferase and luciferin results in peak luminescence within 3 seconds after mixing, which then tapers and levels off after 1 minute [1], [2], [9]. Light measurements for this experiment were integrated 2 minutes 5-sec after the ATP and luciferase/luciferin solution mixed for 20 seconds, when the light flux was approximately constant.

20- μ L of the mixed ATP, luciferase and luciferin solution was dispensed onto a 20×15 -mm² area surrounding the micro chambers. A thin glass cover slip was placed on the solution, starting at one end and tilting the cover slip as it was laid down, so that the excess bioluminescent fluid would disperse. An ST6-A CCD camera, by Santa Barbara Instruments Group was fitted with a Vivatar wide-angle lens and 36-mm close-up ring. The experimental substrates were focused 55-mm below the lens with the aperture set at 2.8. The field of view was about 20×15 -mm². The camera was operated at -20.0°C and shrouded in a darkroom. The resulting images were saved as TIF files. The average CCD counts (which is proportional to intensity) for the areas surrounding the micro-chambers was subtracted as background noise from the CCD counts recorded for the micro-channels, using Scion Image (based on the NIH image software).

4) *Light measurements from the ChemChips with long narrow channels:* The 1.84- μ M firefly luciferase/1.25-mM luciferin solution and the 5.0-mM ATP solutions were prepared as explained above. They were then dispensed into 1-mL aliquots and frozen at -70°C . The two solutions were thawed for 3.5-minutes at 29°C in a dark container, and then mixed in a 20:5 (luciferin/luciferase: ATP) volumetric ratio as before. New 1-mL aliquots of both solutions were

used for each channel array tested. Although freezing these solutions does decrease their activity, and thus total light intensity, all channels were tested with the same decrease in activity by ensuring that the reagents were used after the same thawing time.

The channels filled via capillarity on one end, after dispensing 5- μ L of the mixed ATP and luciferase/luciferin solution onto one side of the channel arrays. The bioluminescence was viewed "end on" at the other side of the channels with the same CCD setup used for viewing the micro-channels. However, a 48-mm close-up ring was used and the ends of the channels were focused 8.75-mm away from the lens in order to have a larger magnification (with a field of view was about $5\text{-mm} \times 3\text{-mm}^2$). A 20-sec light exposure was taken 1.5 min after the luciferin/luciferase & ATP solutions were mixed. Images were saved in TIF format and again analyzed with Scion Image. The light intensity (in CCD counts) from each channel was compared to channel length.

III. RESULTS DISCUSSION

1) *Coating enhancement of micro reaction chambers:*

Fig. 5 shows the CCD images recorded from the bioluminescence on the chromium and silver coated (respectively) substrates. Fig. 4 shows the light intensity from the different reflective coatings (measured as average CCD counts) for certain size reaction chambers. The higher intensity values occur for the deeper wells due to the integration of the light generating media as predicted by the Beer-Lambert law. The intensity/volume slope indicates the effectiveness of increasing intensity with slight increases in volume. Steeper slopes occur for smaller windowed micro reaction chambers and for substrates with higher reflectance at $\lambda = 560\text{-nm}$ light. Comparison of the slopes (intensity/volume) is seen in TABLE 1.

2) *Light intensity varying as a function of channel length:* In observing the capillary action of the bioluminescent fluid into the channels, we noticed that the narrower channels filled at a slower rate than the wider ones. This was due to the hydrophobicity of the PDMS walls. As the channels got narrower, the ratio of hydrophobic PDMS wall surface area to the hydrophilic glass surface area increased, reducing the surface tension driving the capillarity.

Fig. 6 shows the bioluminescent light images seen by the CCD from the ends of the channels. Comparison of the intensity versus sample volume (Fig. 7) resulted in an intensity/volume of 101 CCD counts/nL for the 250-mm wide channels and 79 CCD counts/nL for the 200-mm wide channels. The P value between these two slopes was 0.08. Comparison of the intensity/volume for the other channel widths did not show any correlation for any of the graphs. This inconsistency could have been due to the poor capillary filling in the smaller channels (as described above). This would cause lower than expected intensity measurement because the channel would only be partially filled. Initially, the PDMS channels were left hydrophobic (un-oxidized) in

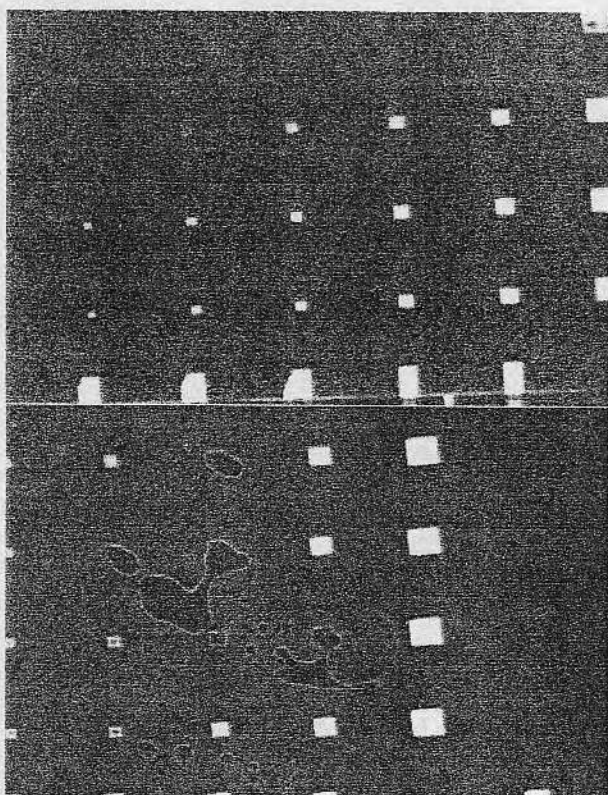


Fig. 5. 20-Sec Integration Of Bioluminescence for a Waters Etched 250- μ m.

Top) Coated With Cr. Showing the 750, 500, 400, 300, 250, and 200- μ m wide squares.

Bottom) Coated with Ag. Showing the 750, 500, 400, 300, and 250. The 10- μ m wide chambers to the right of the 750- μ m chambers are too small to be picked up by the CCD.

TABLE 1
COMPARISON OF INTENSITY/VOLUME SLOPES FROM Fig. 4

μ RC Width (μ m)	Intensity/Volume Slope Ratio Chromium Verses Silicon	P Value	Intensity/Volume Slope Ratio Silver Verses Chromium	P Value
750	302	0.00001	1884	3.55E-18
500	237	0.002	831	3.71E-09
400	494	0.004	520	3.22E-05

Comparison of the Intensity/Volume slopes between the reflective surfaces had P values ≥ 0.28 for square chamber sizes less than 400- μ m.

order to be able to clean and reuse the arrays during the bioluminescent measurements. Because the PDMS was left hydrophobic, the capillarity did not work well for the smaller channels. The capillarity can be improved for this experiment by oxidizing the PDMS in a plasma cleaner as was done by Whitesides et al. This will, however, permanently seal the PDMS channels.

Error could also have been introduced by light cross talk between channels occurring from internal reflection within the glass. This could have occurred even though the glass was on a black matte surface during the light measurements. The cross talk might be eliminated in the future by using chromium or silver coated glass slides. This might also improve the signal intensity.

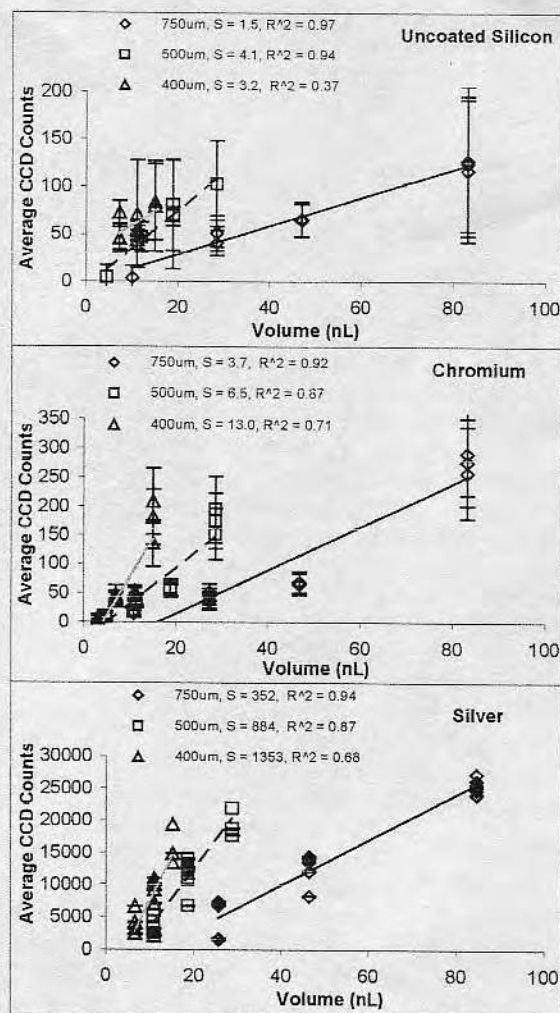


Fig. 4. Average CCD Counts from the 20-Sec Integrated CCD Reading for Bioluminescence in Micro Reaction Chambers with Different Reflective Coatings.

Data was plotted in sets for the same viewing area (or width of micro reaction chamber). For each set of data (wells with same width and coating), the increasing volume occurs from the three etch depths used (250-nm, 100-nm and 50-nm). The higher intensity values occur for the deeper wells. The intensity/volume slope indicates the effectiveness of increasing intensity with slight increases in volume. Steeper slopes occur for smaller windowed micro reaction chambers and for substrates higher reflectance at $\lambda = 560$ -nm light. Comparison of the slopes (intensity/volume) is seen in TABLE 1.

The poor correlation of light intensity and sample volume for the smaller channels could have also been due to the difficulty in obtaining a precisely focused image of the smaller channels. Selecting the area to measure average intensity (using Scion Image) for each channel was somewhat subjective when any blur in the image for the small channels occurred. Precise coupling of the channels to the CCD will continue to be an issue. Large camera lenses are impractical for developing a hand held bioluminescent-based POC. Eventually, a linear CCD array could be fabricated right onto the ChemChip with minimal coupling error.

IV. CONCLUSION

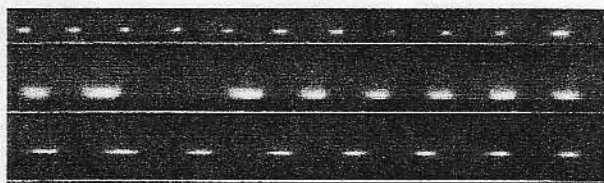


Fig. 6. CCD Images of the Bioluminescent Light from PDMS Channels of Various Lengths - "End on" View

Top) 12.0-mm long channels. From left to right, two 75- μ m, five 50- μ m and two 25- μ m wide channels are seen.

Middle) 11-mm long channels. Three 250- μ m, and five 200- μ m wide channels are seen.

Bottom) 2-mm long channels. Two 200- μ m, five 150- μ m, and one 100- μ m wide channels are seen.

Based on these experiments, silver coated substrates have the greatest potential to enhance light output for small sample volumes. The largest silver coated chambers were able to reach CCD counts of 30,000 for sample volumes of about 85-nL. These values of intensity were not obtained in the PDMS channels except at volumes of about 200-nL. However, the output in the channels may be improved by coating the walls (or some of the walls) with silver. This however, will not double the effective transmittance length unless there is a back reflective wall designed into the channels.

The next step in the development of the bioluminescent-based ChemChip will be to perform calibration curves of light output at low concentrations of ATP (in the μ M range). After that, we will be determining ways of preparing and lyophilizing the bioluminescent compounds within the channels and then sealing the channels without inactivating the enzymes. (Methods such as anionic bonding and UV or high temperature curing adhesives would denature the enzymes.)

Depending on the microfabrication procedure used to build it, the ChemChip can easily be integrated with other MEMS technology. An example of integrating the ChemChip with other MEMS technology is in the area of microneedles. The increased light observed for long narrow channels can also be used to effectively design a bioluminescent micro-needle. These microneedles can be incorporated into the ChemChip or designed to have the bioluminescent reaction occur within one or more of the lumens [10] [11]. With increased sensitivity, smaller amounts of sample fluids are needed for accurate analysis. A 0.05-mL sample size can be drawn by micromachined needles, which can painlessly access small amounts of body fluid to be analyzed via bioluminescence.

By integrating bioluminescence with other analytical methods, using MEMS technology, inexpensive yet comprehensive POC metabolic analytical panels can be created.

ACKNOWLEDGMENT

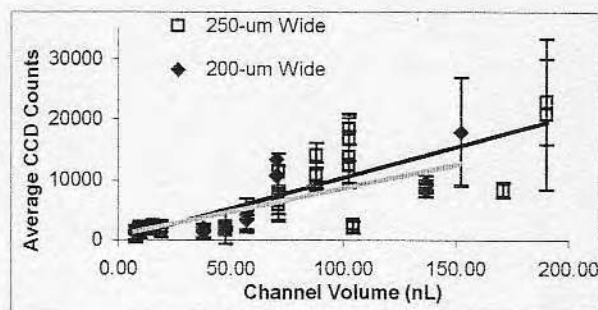


Fig. 7. Average CCD Counts for 250- μ m and 200- μ m Wide Channels at Various Volumes

The slope of CCD counts/Volume is 101 counts/nL ($R^2 = 0.6128$) for channels 250- μ m wide and 79 counts/nL ($R^2 = 0.69$) for channels 200- μ m wide. Although the R^2 values are low, comparison of the slopes result in a P value of 0.08.

D. B. thanks Rupert Davies of Dr. Andrade's 4-M Lab Group for helping determine and make the proper bioluminescent solutions needed.

REFERENCES

- [1] S. Brodin and G. Wettermark, *Bioluminescence Analysis*. VCH Publ., 1992.
- [2] A. Campbell, *Chemiluminescence*, VCH Publ., 1989.
- [3] D. Min, J. Andrade, R. Stewart, "Specific Immobilization of *in Vivo* Biotinylated Bacterial Luciferase and FMN:NAD(P)H Oxidoreductase," *Anal. Biochem.*, vol. 270, pp. 133-139, 1999.
- [4] G. Weinhausen, M. DeLuca, "Bioluminescent Assays of Picomolar Levels of Various Metabolites Using Immobilized Enzymes," *Anal. Biochem.*, vol. 127, pp. 380-388, 1982.
- [5] I. Levine, *Physical Chemistry 4th ed.*, McGraw-Hill, 1995, pg. 685.
- [6] J. Brazzle, D. Bartholomeusz, R. Davies, J. Andrade, R. Wagenen, B. Frazier, "Active Microneedles With Integrated Functionality," *Solid State Sensors and Actuators Conference*, Transducers Research Foundation, Hilton Head S.C. USA, June 4-8, 2000.
- [7] D. Cuffy, J. McDonald, O. Schueller, G. Whitesides, "Rapid Prototyping of Microfluidic Systems in Poly(dimethylsiloxane)," *Anal. Chem.*, vol. 70, no. 23, pp. 4974-4984, December 1, 1998.
- [8] J. Eu, C. Wang, J. Andrade, "Homogeneous Bioluminescence Assay for Galactosuria: Interference and Kinetic Analysis," *Anal. Biochem.*, vol. 271, pp. 168-176, 1999.
- [9] S. Ford, F. Leach, "Improvements in the Application of Firefly Luciferase Assays," in *Bioluminescence Methods and Protocols*, vol. 102, R. LaRossa Ed. Humana Press, 1998, pp. 3-20.
- [10] J. Brazzle, I. Papautsky, and A. B. Frazier, "Fluid-coupled metallic microfabricated needle arrays," in *Proc. SPIE Micro Fluidic Devices and Systems*, Santa Clara, CA, Sep. 21-24, pp. 116-124, 1998.
- [11] J. Brazzle, S. Mohanty, and A. B. Frazier, "Hollow Metallic Micromachined Needles with Multiple Output Ports," *SPIE Micro Fluidic Devices and Systems*, Santa Clara, CA, Sept. 20-21, pp. 257-266, 1999.

within 1% accuracy during the 3 second exposure with the CCD (as verified by PMT measurements). We determined $\bar{I}_{FFL}(\vec{r})$ by CCD measurements and $\bar{I}_{FFL}(\lambda)$ by spectrometer measurements. Equations 3, 5, and 6 were used to determine $I_{FFL}(t)$ where $I_{FFL}(t=3.5\text{min})$ replaced $I_{LED}(t)$ and $O_{Detector}(t=3.5\text{ min})$ was measured. Radiance $R_{FFL}(t)$ was determined by equation 4.

RESULTS AND DISCUSSION

Measurement errors were determined by standard propagation of error methods. The error in R_{FFL} for the PMT was large because the data used for $S_{PMT}(\lambda)$ was not high resolution, which affected the error in the integration of $\bar{I}(\lambda)\bar{S}_{PMT}(\lambda)d\lambda$ in equation 5.

The radiance measurements in Table 1 show that once a device is calibrated, bioluminescence can be recorded in units that allow comparisons independent of instruments and setup. Standard equipment usually available to those researching luminescence, was used for calibration. Standardizing luminescent measurements in units of radiance, which accounts for collection angle, would allow better comparisons of luminescent assays between different instruments and labs.

Table 1. Conversion Constants, Collection Angle, Irradiance, and Radiance for ATP/FFL bioluminescence measurements at $t = 3.5\text{ min}$

I_{LED} and $k_{detector}$ Values	Value	Error	Irradiance (nW/cm^2)	Value	Error
I_{LED} (nW/cm^2)	1.27	0.07	I_{FFL} Si detector	5.3	0.3
k_{PMT} (RLU/nW)	3.0	0.9	I_{FFL} PMT	5	1
k_{CCD} (CCDcounts/nW/s)	46×10^7	9×10^7	I_{FFL} CCD	0.3692	0.0002
Collection Angles Ω (sr)			Radiance ($\text{nW}/\text{cm}^2/\text{sr}$)		
LED (Fig1 (a))	0.03317	0.00002	R_{LED} Si	1020	60
ATP/FFL Si	1.893	0.002	R_{FFL} Si	2.8	0.2
ATP/FFL PMT	1.928	0.002	R_{FFL} PMT	2.4	0.6
ATP/FFL CCD	0.1309	0.0001	R_{FFL} CCD	2.8	0.1

ACKNOWLEDGMENTS

Dr D.A. Christensen and Dr S.M. Blair of the University of Utah for the use of their detection equipment and guidance on the experimental setup.

REFERENCES

1. Saleh BEA, Teich MC. Fundamentals of Photonics. New York: John Wiley & Sons, 1991: 44.
2. Ryer A. Light Measurement Handbook, Newburyport, MA: International Light, Inc. 1997: 26-42.
3. Créton R, Jaffe, L. Chemiluminescence microscopy as a tool in biomedical research. Biotechniques 2001; 31:1098-105.

PHOTODETECTOR CALIBRATION METHOD FOR REPORTING BIOLUMINESCENCE MEASUREMENTS IN STANDARDIZED UNITS

DA BARTHOLOMEUSZ, JD ANDRADE

Dept of Bioengineering, University of Utah, Salt Lake City Utah 84112-9202, USA

Email: d.bartholomeusz@m.cc.utah.edu

INTRODUCTION

Bioluminescence measurements are reported in relative light units (RLU), which are dependent on the specific detector used and its operating conditions. In order to compare bioluminescent measurements from different detectors and assays, or to determine the quantum efficiency of a particular assay, photodetectors need to be calibrated such that measurements are reported in radiance ($\text{W}/\text{cm}^2/\text{sr}$). This allows intensity measurements to be expressed in units normalized to the collection angle and independent of the device. We explore a calibration method using a diffused light emitting diode (LED) as a light source standard. The uniform light source is focused onto a silicon photodiode detector whose spectral calibration is traceable to a National Institute of Standards and Technology (NIST) standard. The intensity of the focused light source is calibrated in W/cm^2 as a function of the solid collection angle. The calibrated light source is then used to calibrate a photomultiplier tube (PMT)-based luminometer and a charge-coupled device (CCD) in $\text{W}/\text{cm}^2/\text{sr}$. The method accounts for spectral properties of detector responsivities and light sources.

METHODS

In order to calibrate a detector, the intensity of a source $I(t, \vec{r}, \lambda)$ (in irradiance units of W/cm^2) must be known as a function of time t , position at the detection plane $\vec{r} = (x, y)$, and wavelength λ (Fig. 1). An LED operating at a steady state temperature with a constant current source and a diffuser plate is used in order to define the intensity as a function of t, \vec{r} , and λ . In this case, $I(t)$ is a constant value for all λ and \vec{r} due to the constant temperature and current. Since the Lambertian diffuser plate averages any variance in $I(\lambda, \vec{r})$ due to uneven temperatures on the surface of the LED, $I(\lambda)$ can be integrated over the emission spectrum independent of \vec{r} . $I(t, \vec{r}, \lambda)$ can be further simplified by normalizing $I(\vec{r})$ and $I(\lambda)$, according to their respective peak intensities in position and wavelength. Thus, $I(t, \vec{r}, \lambda)$ for the LED source described becomes:

$$I_{LED}(t, \vec{r}, \lambda) = I(t)I(\vec{r})I(\lambda) = I_{LED}(t)\bar{I}(\vec{r})\int_{\lambda} \bar{I}(\lambda)d\lambda \quad \text{Equation 1.}$$

The optical power of the source at the detection plane, $P(\lambda)$ (in radiant flux units of watts), is the integration of the intensity, I , normal to the detector over the area, A , of the detector (equation 2).¹ O_{Si} is the calibrated silicon detector output from incident source power, P , on the detection plane is a function of the detectors

normalized spectral responsivity, $\bar{S}_{Si}(\lambda)$ (equation 3). All detectors in this experiment were normalized to their responsivities at 555 nm, the peak wavelength of the LED. The second half of equation 3 combines $P(\lambda)$ and $I(t, \vec{r}, \lambda)$ in the calculation of O_{Si} .

$$P(\lambda) = \int_A I_{LED}(t, \vec{r}, \lambda) dA \quad \text{Equation 2.}$$

$$O_{Si}(t) = \int_{\lambda} P(\lambda) S(\lambda) = I_{LED}(t) \int_A \bar{I}(\vec{r}) dA \int_{\lambda} \bar{I}(\lambda) \bar{S}(\lambda) d\lambda \quad \text{Equation 3.}$$

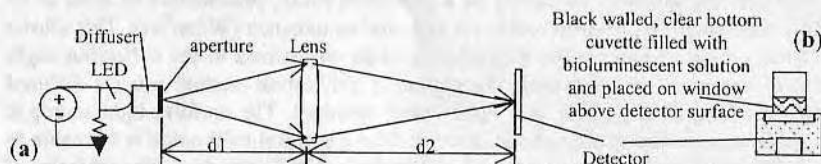


Figure 1. Setup for measuring O_{Si} and (a) calibrating the LED light standard for subsequent calibration of the PMT based luminometer and CCD detector and (b) subsequent bioluminescence measurements

Fig. 1 (a) shows the experimental setup used to measure O_{Si} and calibrate the LED source standard along with subsequent detector calibrations. A constant voltage source from a DC power supply across a precision resistor was used to create a constant current across the LED (555 nm peak wavelength intensity, 24 nm full half width maximum, Fairchild HLMP-D600). This LED was used because its spectral emission fell within that of the firefly luciferase bioluminescence, which was verified later. The light from the LED was diffused through a 5 mm diameter Lambertian diffuser plate (Edmund Optics A46-162). An aperture on the diffuser plate was created by using photolithography to etch a 250 μm hole in aluminum that was evaporated onto the clear side of the diffuser plate. This provided a small enough source such that the diameter of the source divided by d_1 was much less 0.02, effectively acting as a point source.² d_2 was selected such that the maximum incident angle, θ , was less than 5° . This ensured that over 99% of the light was within the $\pm 5^\circ$ radiance response curve for which the photodetector was calibrated.² d_2/d_1 was chosen such that all of the magnified image of the uniform source easily fit within the detector area for all detectors. Since $d_1 \geq 5 \times$ diameter of lens (focal length = 50.2 mm), the solid collection angle, Ω , could be approximated as the area of the lens aperture area divided by the square of d_1 (less than 1% error).²

A calibrated silicon photodetector (Newport 818-SL) with a known responsivity, $S(\lambda)$, traceable to a NIST standard, along with a CCD (Santa Barbara Instruments, ST-7E with a Kodak KAF-0401E CCD) was used to solve for the intensity of the LED source standard for the specific set-up in Fig. 1(a). O_{Si} was measured by the calibrated photodetector. The normalized intensity as a function of

position, $\bar{I}(\vec{r})$, was determined by CCD measurements and the normalized intensity as a function of wavelength, $\bar{I}(\lambda)$, was determined with a spectrometer (Jobin Yvon Spex #HR-460). After determining O_D , $\bar{I}(\vec{r})$, and $\bar{I}(\lambda)$, $I_{LED}(t)$ was calculated from equation 4. $I_{LED}(\vec{r})$ from equation 1 was then determined. The radiance, $R(\vec{r})$, of the LED standard was then determined by equation 4, where Ω is the solid collection angle. For a uniform source, $I(\vec{r})$ and $R(\vec{r})$ are both constant. The LED source had a gaussian distribution, giving radiance as follows:

$$R_{Source}(t, \vec{r}) = I_{Source}(t, \vec{r}) / \Omega \quad \text{Equation 4.}$$

Once the radiance of the LED source standard was determined, the same setup shown in Fig. 1 was used for calibrating the PMT based luminometer (Turner Desing 20/20 with Hamamatsu R6427 PMT). The operation of the luminometer allows the user to adjust the sensitivity, which adjusts the amplification voltage of the PMT. Because of this, each sensitivity setting would have to be calibrated for any given PMT. Here we only performed one calibration for a single sensitivity setting (4.2%). The calibration of the PMT was based on the following modification of equation 3,

$$O_{PMT}(t) = k_{PMT} I_{LED}(t) \int_A \bar{I}(\vec{r}) dA \int_{\lambda} \bar{I}(\lambda) \bar{S}_{PMT}(\lambda) d\lambda \quad \text{Equation 5.}$$

where O_{PMT} is the output of the luminometer (in RLU), k_{PMT} is the conversion factor of RLU/nW at the specific sensitivity settings, and $\bar{S}_{PMT}(\lambda)$ is the normalized spectral responsivity of the PMT. Since O_{PMT} was constant for all $I_{LED}(t)$, $\bar{I}(\vec{r})$, and $\bar{I}(\lambda)$ was known from the LED calibration, we then solved for k_{PMT} .

The calibration of the CCD was similar to that of the PMT, but accounts for the integration of the charge accumulation in the CCD wells during the exposure. Thus, the calibration of the CCD is as follows:

$$O_{CCD}(\Delta t) = k_{CCD} I_{LED} \Delta t \int_A \bar{I}(\vec{r}) dA \int_{\lambda} \bar{I}(\lambda) \bar{S}_{CCD}(\lambda) d\lambda \quad \text{Equation 6.}$$

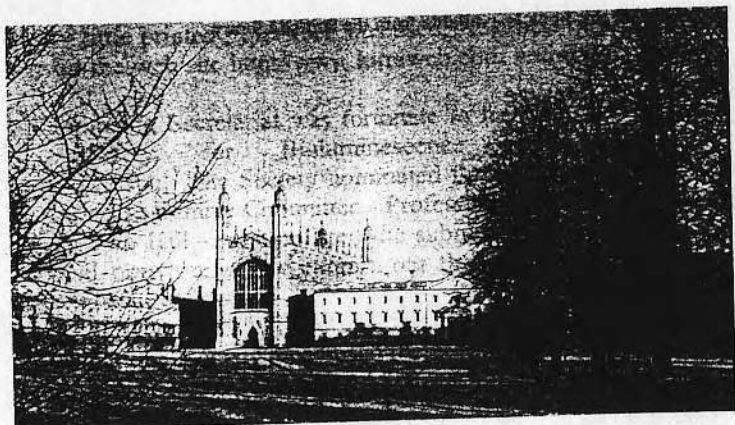
where O_{CCD} is the output of the CCD (in CCD counts), k_{CCD} is the conversion factor of CCDcounts/nW/s at the specific temperature setting of the CCD (-6.9°C), and $\bar{S}_{CCD}(\lambda)$ is the spectral responsivity of the CCD (in V/incident watts) normalized at 555nm. Since the light source is constant for all t , $O_{CCD}/\Delta t$ (where Δt is the integrated shutter exposure time) was used to solve for k_{CCD} .

k_{PMT} and k_{CCD} can be determined for all respective detector operating conditions using the method described above. Once k_{PMT} and k_{CCD} were known for their respective detector operating conditions in this example, we calculated the irradiance and radiance of a 250 μL volume of an ATP/firefly luciferase (FFL) bioluminescence assay with the setup as seen in Fig. 1(b). [1 mM ATP (Sigma), 1 mM Luciferin (BioSynth), 0.11 mg/mL Luciferase (Promega), 250 mM Mg^{2+} (Sigma), 0.8 mg/mL BSA (Sigma)].

Measurements of the three detector outputs were performed 3.5 min after mixing the ATP into the bioluminescent solution, such that the intensity was constant

BIOLUMINESCENCE & CHEMILUMINESCENCE

Progress & Current Applications



editors

Philip E. Stanley

Cambridge Research & Technology Transfer Ltd., England

Larry J. Kricka

*Department of Pathology & Laboratory Medicine
University of Pennsylvania School of Medicine, USA*

World Scientific
New Jersey • London • Singapore • Hong Kong

Published by

World Scientific Publishing Co. Pte. Ltd.

P O Box 128, Farrer Road, Singapore 912805

USA office: Suite 1B, 1060 Main Street, River Edge, NJ 07661

UK office: 57 Shelton Street, Covent Garden, London WC2H 9HE

British Library Cataloguing-in-Publication Data

A catalogue record for this book is available from the British Library.

BIOLUMINESCENCE & CHEMILUMINESCENCE: PROGRESS & CURRENT APPLICATIONS

Copyright © 2002 by World Scientific Publishing Co. Pte. Ltd.

All rights reserved. This book, or parts thereof, may not be reproduced in any form or by any means, electronic or mechanical, including photocopying, recording or any information storage and retrieval system now known or to be invented, without written permission from the Publisher.

For photocopying of material in this volume, please pay a copying fee through the Copyright Clearance Center, Inc., 222 Rosewood Drive, Danvers, MA 01923, USA. In this case permission to photocopy is not required from the publisher.

ISBN 981-238-156-2

This book is printed on acid-free paper.

Printed in Singapore by Uto-Print



ISBC 2004

Bioluminescence & Chemiluminescence

Progress and Perspectives

edited by

Akio Tsuji
Showa University, Japan

Masakatsu Matsumoto
Kanagawa University, Japan

Masako Maeda
Showa University, Japan

Larry J Kricka
University of Pennsylvania School of Medicine, USA

Philip E Stanley
Cambridge Research & Technology Transfer Ltd, UK



METHOD FOR IMPLEMENTING BIOLUMINESCENCE-BASED ANALYTICAL ASSAYS IN NANOLITER VOLUMES

DA BARTHOLOMEUSZ, RH DAVIES, TSM YANG, JD ANDRADE
Dept of Bioengineering, University of Utah, Salt Lake City UT 84107, USA

INTRODUCTION

Bioluminescence-based analytical assays were used to measure various analytes in nanoliter sample volumes. Nanoliter volumes of multiple bioluminescent analytical assays were deposited in an array format and lyophilized. ATP-firefly luciferase (FFL) and NADH-bacterial luciferase (BL) platform reactions were compared. We achieved parallel sample delivery via sample-hydrated membranes. A CCD camera measured the luminescent kinetics for each assay. These miniaturized assays and instruments can be prepared as micro-analytical systems to operate in point-of-care (POC) diagnostic devices.

METHODS

ChemChip fabrication

We built arrays of clear bottom reaction wells, or ChemChips, consisting of 5x5 arrays of 1 mm diameter holes spaced 2 mm apart. The holes were cut in 15 mm squares out of 0.180 mm thick adhesive backed vinyl film with a knife plotter. The array patterns were sealed to 15 mm square glass cover slips after manually removing the cut holes. The glass cover slips became the clear bottom for the 140 nL wells (Fig. 1A).

Reagents and samples

ATP, NADH, Lactate, and Galactose assays were formulated according to Table 1. Mixed analyte samples were made at various concentrations in 50 mM Trizma buffer (pH 8.0). Lactate and Galactose assays were measured using samples without ATP and NADH since they interfere with their respective competition and production reactions.

Table 1. Analytical assay recipes

Reagents	ATP	Galactose	Reagents	NADH	Lactate
FFL -Promega	5 μ M	3.3 μ M	FMN -Sigma	200 μ M	100 μ M
Luciferin -Biosynth	0.1 mM	0.0 67mM	RCHO -Sigma	200 μ M	100 μ M
CoA -Fluka	100 μ M	67 μ M	BL -U of Utah	2 μ M	1 μ M
Mannitol -Pfanstiel	0.4 M	0.27 M	Oxidoreductase -Roche	2.4 u/mL	1.2 u/mL
40kD Dextran -Pharmacia	1mg/mL	0.67 mg/mL	Sucrose - Pfanstiel	0.5 M	0.5 M
8kD PEG -Sigma	5mg/mL	3.3 mg/mL	8kD PEG -Sigma	2 mg/mL	2 mg/mL
BSA -Sigma	30 μ M	20 μ M	BSA -Sigma	5 mg/mL	5 mg/mL
ATP -Sigma		5 μ M	GPT -Sigma		125 μ g/mL
Mg ⁺⁺ -Sigma		50 μ M	Glutamate -Sigma		2 mM
Galactokinase -Sigma		0.2 u/mL	Lactate Dehydrogenase -Sigma		250 μ g/mL
			NAD ⁺ -Sigma		1 mM



Figure 1. A) Empty ChemChip, B,C) Reagent deposition system

Reagent deposition

Individual ChemChip wells were filled with reagent cocktails via a computer controlled XYZ stage with a syringe pump and solenoid dispensing system (Fig. 1B,C). A miniature solenoid valve with a 0.002" nozzle (INKX0516350AA, The Lee Company) dispensed reagents in 10 ms pulses, pressured at 8 PSI. The drops were calibrated at 360 ± 10 nL. A tray of 25 chips was cooled to less than -60 °C using dry ice (Fig. 1C shows the chips on the cold plate), allowing the reagent droplets to freeze within seconds of dispensing. This process prevented evaporation and maintained reagent stability prior to lyophilization.

Lyophilization

Lyophilization was performed in two stages in a VirTis Genesis 12 pilot plant lyophilizer. The chips were placed in the sample chamber of the lyophilizer, which had been previously cooled to at least -50 °C. Primary lyophilization began when the sample chamber was connected to the condenser chamber cooled to -70 °C with a system pressure below 100 mTorr. Primary lyophilization was performed for 48-72 hr. Secondary lyophilization was then performed for 12-24 hours after changing the sample chamber to 25 °C.

Simple sample delivery

25 μ L samples were dispensed on the center of 14 mm diameter circles Whatman qualitative membrane filters clamped to the center of the ChemChips. Since the membranes hydrate uniformly, less than 1 μ L of the 25 μ L sample was delivered to each of the 25 wells. Given a 2 mm well spacing and a 0.18mm thick membrane, only 510 nL of sample was available to each well. The sample wicked along the membrane and into each well, whereupon the reagents rehydrated and bioluminescence reactions began. Since reagent drops were larger than the volume of the wells, a convex meniscus formed above each well. This convex structure, porous and hydrophilic in nature after lyophilization, facilitated drawing the sample from the membrane into each well without the risk of bubble formation.

Detection

An Andor DV-434 CCD was used to take a series of six 30-s exposures to record the bioluminescence activity for each assay (CCD temp = -50 °C, binning = 4×4 pixels). CCD images can be seen in Fig. 2. Although we used a sensitive CCD camera, some of the assays were bright enough to see with the human eye. These assays produced

an estimated 10 nanoWatts/steradian/cm².¹ Such a signal produces a current signal of about 50 pA on the CCD. This is about 50 times greater than the dark current for the less expensive photodiode arrays (Hamamatsu S8593 and S8550) (assuming a collection angle of 1steradian, an area of 5.3 mm², and a photosensitivity of 0.3 A/W on the photodiode arrays) These arrays would enable the ChemChip to be implemented in a less expensive POC diagnostic device.

Data Analysis

The native Andor data files were opened in ImageJ (from NIH) where a macro integrated the CCD counts across the area of each well for each exposure. We used Matlab to sort the data by analyte and sample concentration. Calibration curves for ATP, NADH, and Lactate assays were created by time integrating the CCD counts across each well. Time integrated CCD counts were then averaged across all 5 rows for each column of analyte. An average integration was also taken across multiple chips that were tested at each sample concentration. The calibration curve for the Galactose assay was based on the area integrated CCD counts at $t=180$ s, divided by the area integrated CCD counts at $t=30$ s (the brightest exposure period).

RESULTS

Fig 3 shows the kinetics for the ATP assays. Fig. 4 shows assay calibration curves. The estimated detection limit for each assay was as follows: 0.51 picomoles ATP $\pm 19\%$, 5.1 picomoles NADH $\pm 21\%$, 5.1 picomoles Galactose $\pm 26\%$, and 51 picomoles Lactate $\pm 22\%$.

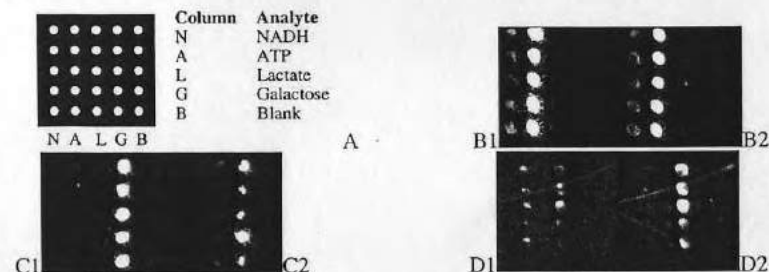


Figure 2. CCD images of luminescent ChemChip arrays

A) Bioluminescence assays were dispensed in separate columns for replicate data (5 rows per column). B1) NADH and ATP at 1 and 0.1 mM, respectively. B2) NADH and ATP at 0.01 and 0.001 mM, respectively. This is dimmer than B1 due to lower concentration of analytes. C1) Galactose assay (1 mM sample) at first 30 s exposure. C2) Galactose assay (1 mM sample) at sixth 30 s exposure. This competition luminescence dims with time. D1) Lactate assay (10 mM sample) at first 30 s exposure. (Streaks of light across are due to a cracked cover slip). D2) Lactate assay (10 mM sample) at sixth 30 s exposure. Being a production assay, the luminescence increases with time.

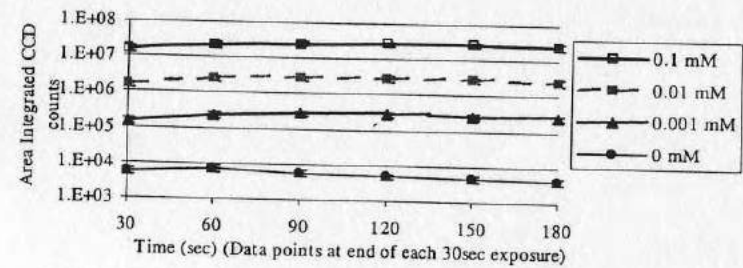


Figure 3. ATP kinetic data averaged over 3 chips, 5 rows/chip

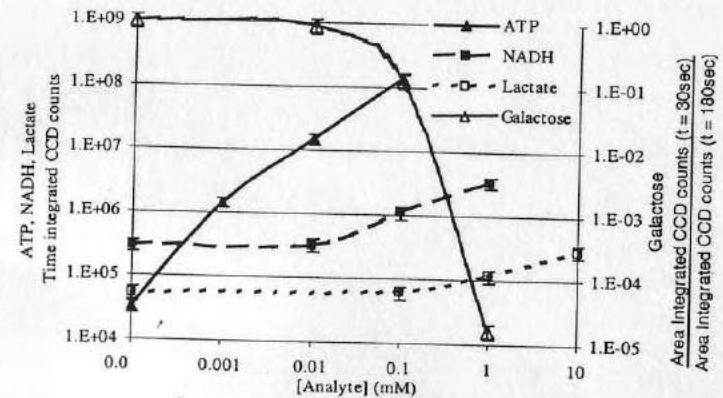


Figure 4. Analyte calibration curves

SIGNIFICANCE

The ChemChip system will provide comprehensive diagnostic and monitoring panels for basic and clinical research, and for personal disease and health management. These systems would provide rapid results, facilitate patient empowerment, and reduce health care costs. The development of panels appropriate to specific clinical research areas will greatly facilitate such research, due to the ease of use, low cost, and multi-parametric data generation of the ChemChip systems.

ACKNOWLEDGMENTS

We acknowledge the support of NIH RFP#PAR01-057 Project#1R21RR17329, Technology Development for Biomedical Applications Grant, and our industrial partners. We also thank Dr. J. Harris of the University of Utah for use of the CCD.

REFERENCE

- 1 Bartholomeusz DA, Andrade JD. Photodetector calibration method for reporting bioluminescence measurements in standardized units. *Luminescence* 2002; 17:77-115.

Xurography: Rapid Prototyping of Microstructures Using a Cutting Plotter

Daniel A. Bartholomeusz, Ronald W. Boutté, and Joseph D. Andrade

Abstract—This paper introduces xurography, or “razor writing,” as a novel rapid prototyping technique for creating microstructures in various films. This technique uses a cutting plotter traditionally used in the sign industry for cutting graphics in adhesive vinyl films. A cutting plotter with an addressable resolution of 10 μm was used to cut microstructures in various films with thicknesses ranging from 25 to 1000 μm . Positive features down to 35 μm and negative features down to 18 μm were cut in a 25 μm thick material. Higher aspect ratios of 5.2 for positive features and 8 for negative features were possible in a 360 μm thick material. A simple model correlating material properties to minimum feature size is introduced. Multilayered microstructures cut from pressure sensitive and thermal activated adhesive films were laminated in less than 30 min without photolithographic processes or chemicals. Potential applications of these microstructures are explored including: shadow masking, electroplating, micromolds for PDMS, and multilayered three-dimensional (3-D) channels. This inexpensive method can rapidly prototype microfluidic devices or tertiary fluid connections for higher resolution devices. [1488]

Index Terms—Laminate object manufacturing, layered microchannels, microelectromechanical devices, microfluidic structures, micromachining, rapid-prototyping.

I. INTRODUCTION

CURRENT interest in microfluidic and microelectromechanical systems (MEMS) for scientific, industrial, and biomedical applications has lead to the development of a number of two- and three-dimensional (2-D and 3-D) microfabrication methods [1]. Initial fabrication methods used integrated circuit (IC) fabrication techniques in semiconductor materials. However, complicated fabrication processes, bonding difficulties, and brittleness of semiconductor material motivated alternative microstructure fabrication techniques and rapid prototyping processes.

Current commercial rapid prototyping methods for microstructures include: micromolding in polydimethylsiloxane (PDMS) [2]–[9], laser ablation [10]–[14], stereo lithography [15], micropowder blasting [10], hot embossing [4], [16], and micromilling [17]. Due to its simple fabrication and bonding techniques, micromolding in PDMS has become a common prototyping microfluidic method in the laboratory environment [2], [3], [6]. Other advantages include low material costs, high

resolution capabilities (down to 30 nm), gas permeability, and optical transparency. Micromolded PDMS structures are typically made by casting the PDMS on photolithographically patterned photoresist. Epon SU-8 photoresist is commonly used because it is capable of producing micromolds as thick as 1 mm with aspect ratios up to 20 [18]. However, even when using SU-8 patterns, PDMS molded microstructures can only have aspect ratios ranging from 0.05 to 2 [3] unless the PDMS is supported. Patterning SU-8 microstructures requires standard photolithographic masks, chemicals, and procedures which involve long pre and post bake development steps. However, once a micromold is created, PDMS structures can be repeatedly molded. Unfortunately, any design change requires a repeat of the long photolithographic process. Alternative photomasks with features down to 15 μm have been used to shorten prototyping time to less than 24 hours [2], [7], but the rate limiting step is still the photolithographic process.

Other prototyping methods such as micropowder blasting and laser ablation directly build microstructures without photolithography. Micro-powder blasting is capable of features $>100 \mu\text{m}$ in hard materials, such as glass, with aspect ratios up to 1.5 (www.micronit.com). Laser ablation produces features on the order of sub-microns ($>100 \text{ nm}$) [19], with an aspect ratio up to 10 [20]. Channels made by these methods are sealed with adhesive films [11]–[14], PDMS layers [21], or anodic bonding. Micronics Inc. (Redmond, WA) has even developed a proprietary method for aligning laser-cut 3-D channels in multiple layers of adhesive backed polymer films [11], [12]. Stereo lithography also builds microstructures directly, with features sizes $>1 \mu\text{m}$ [22] and aspect ratios up to 22 [20]. These techniques require expensive fabrication equipment which makes it difficult for in-house prototyping.

Many features for microfluidic applications do not necessarily need the high resolution capabilities used by IC fabrication techniques. Characteristic dimensions for micropumps, valves, and sensors range from 100 μm –50 mm [23]. Micro-filters and reactors range from 10 μm –10 mm and microanalysis systems range from 1–100 mm [23]. Micro-needles and microfluidic channels range from 1–100 μm wide [2], [24], but can go as high as 1000 μm and still maintain sub microliter volumes depending on channel depth. Micro-channels for whole blood applications can clog when hydraulic diameters are less than 50 μm [25].

Here, we present a rapid and inexpensive microfabrication technique using a cutting plotter (a plotter fit with a knife blade) that has 10 μm resolution to directly create microstructures down to $\sim 20 \mu\text{m}$ in various polymer films, without photolithographic processes or chemicals. We call this method

Manuscript received December 18, 2004; revised July 15, 2005. This work was supported in part by the NIH RFP#PAR01-057, Project#1R21RR17329, Technology Development for Biomedical Applications Grant, and our industrial partners. Subject Editor A. P. Lee.

The authors are with the Laboratory for the Modeling, Measurement, and Management of the Metabolome (4MLab) at the University of Utah, Salt Lake City, UT 84112 USA (e-mail: dbartholomeusz@gmail.com).

Digital Object Identifier 10.1109/JMEMS.2005.859087

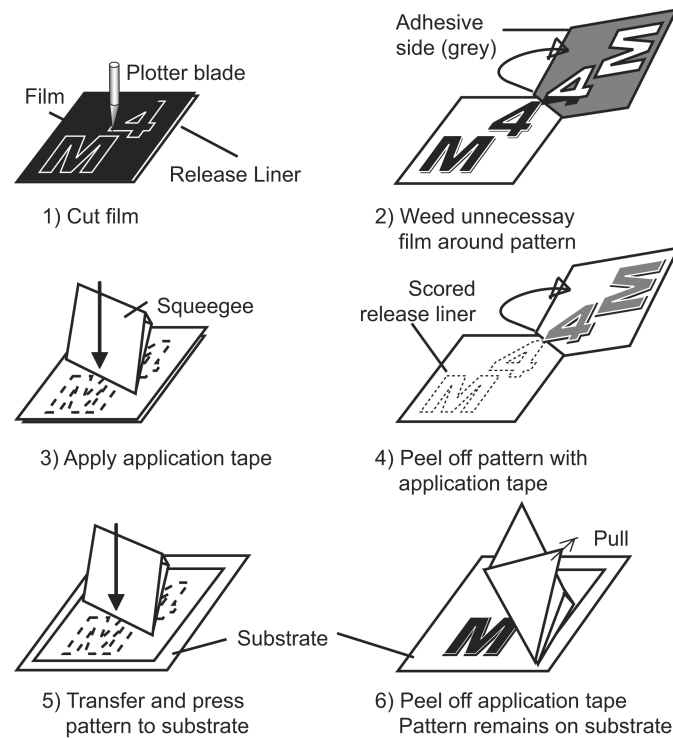


Fig. 1. Pattern transfer method. After cutting, unnecessary parts are peeled off the release liner, or “weeded.” The application tape holds structures in place while transferring. For finer negative structures ($\leq 100 \mu\text{m}$), the entire pattern in step 1 is transferred to application tape *before* weeding. The pattern is then weeded while on the release liner from the backside before transferring. This minimizes adhesive left in negative channels. Another method for small structures ($\sim 100 \mu\text{m}$) with positive and negative features (like serpentine channels in Fig. 2) is to lightly transfer the cut-patterns to the substrate and *then* weed the unnecessary portions. In step 6, pull the application tape at a sharp angle while pressing down with the squeegee at the peeling interface to prevent delicate substrates, like glass cover slips, from breaking.

Xurography, for the Greek root words *Xuron* and *graphē* meaning *razor* and *writing*, respectively.

Positive and negative structures, primarily channels, are xurographically fabricated in polymer films ranging from 25–1000 μm thick. The microstructures can be fabricated to create single layer or 3-D layered channels for microfluidic devices, micro-molds, shadow masks, sensors, and electroplated structures. A method for testing cutting conditions is reported along with a model predicting minimum feature size based on material properties.

II. EQUIPMENT AND MATERIALS

The graphic arts industry often uses a tool called a cutting plotter for cutting the outlines of letters and designs in adhesive backed films when making large retail signs. These adhesive backed films, often vinyl, come in rolls laminated on a release liner. After cutting pattern outlines, the undesired portions of the film are “weeded” off the release liner by hand, leaving the letters and designs in place on the release liner. The remaining graphics are transferred to a substrate (wall, billboard, sign, etc.) with an application tape, which is often a light paper based adhesive tape similar to masking tape. The application tape is then peeled away, leaving the graphics attached to the substrate. Fig. 1 shows this transfer process.

Previously, cutting plotters have been used for macroscale prototyping applications [26]–[28]. However, because plotter

technology has dramatically improved upon resolution, alignment, and user control, microscale prototyping with a cutting plotter is now possible. Manufacturers specify the resolution of the cutting plotters in terms of mechanical and addressable resolution. The mechanical resolution specifies the resolution of the motors, while the addressable resolution is the programmable step size. Most cutting plotters have addressable resolution down to 25 μm , which is the resolution limit of the Hewlett Packard Graphing Language® (HPGL™) driver to print plotter files. For higher plotter resolution, a different driver is required. The repeatability of the cutter is the quantitative measure of the machine’s ability to return to the exact point where a cut initiated, such as occurs when cutting a circle. Cutting plotters control the material feed by friction rollers or sprocket feed spools.

Cutting plotters use different blades for various materials. Blade angles of 30°, 45°, and 60° are common throughout the sign industry. Blade angle is measured from the surface of the material to the blades’ cutting edge. Blade angle and depth determine the amount of uncut material between the blades leading edge. Blade depth is controlled by a depth or force setting, depending on the plotter.

There are three types of cutting methods which cutting plotters use, namely; drag knife, true tangential and emulated tangential. Drag knife cutting uses a swivel blade that follows the cutting path of the feature as it moves relative to the material. This introduces lateral force from the blade at sharp feature corners, which can break the tip when cutting harder or

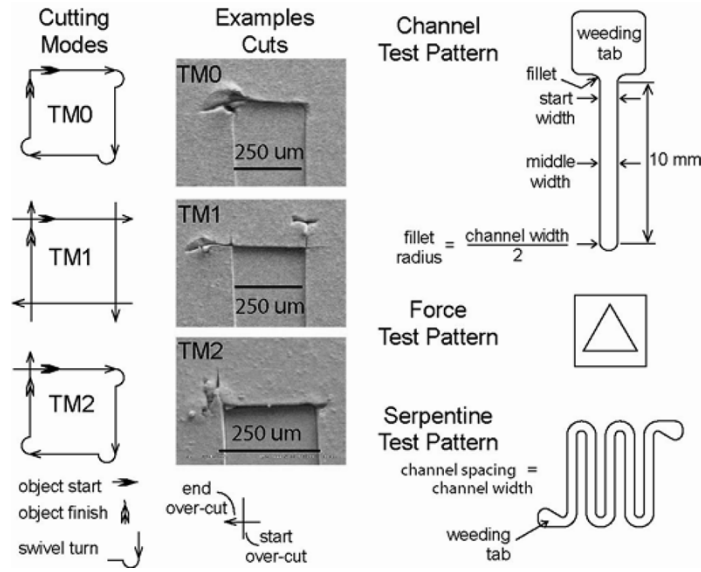


Fig. 2. Cutting modes and test patterns. The blade in TM0 (drag knife mode) pivots at the corners. TM1 (tangential mode 1) cuts each line segment and lifts. The blade then rotates into position as it starts to cut the next line segment. TM2 only applies a start and end overcuts at the object start and finish. Channel width was measured at the start of the channel test pattern near the tab and where the taper leveled off in the middle. The force test pattern is used to determine the proper force to completely cut the material. The serpentine test pattern consisted of channels with equal width and spacing. The smallest serpentine test pattern that successfully weeded determined the minimum feature spacing.

thicker substrates. True tangential cutting controls blade position with an addressable motor. When cutting corners, the blade lifts completely out of the material and rotates to the new direction. Line segments can be over-cut to ensure the material is completely cut from top to bottom at feature corners. This is useful when cutting thick materials. Emulated tangential cutting uses a swivel blade but lifts the blade just to the surface of the material before pivoting on the tip at a feature corner. This reduces lateral force on the blade. Over-cuts in emulated tangential plotters bring the blade into position before initiating a cut and ensure feature corners are completely severed from the rest of the material.

In order to have flexibility for testing xurography on multiple materials, a friction feed cutter with the ability to cut material up to 1 mm thick was needed. Test patterns with round, rectangular, and angled features ranging from 10 μm to 2 mm wide were sent to a few cutting plotter manufacturers. Each manufacturer cut test patterns in sample materials ranging from 50 to $\sim 1\,000\ \mu\text{m}$ thick. Cutting plotters with tangential blades were able to cut rectangles and square patterns better than those with swivel blades. However, those with swivel blades were able to cut circular features down to 50 μm in diameter better than tangential blade machines due to the continuous cutting nature of the swivel blade.

We purchased the FC5100A-75 from Graphtec ($\sim \$4\,000$ USD, www.graphtecusa.com) because it has an addressable resolution of 10 μm (most plotters only go down to 25 μm) and it cut channels less than 100 μm wide with a uniform channel width that surpassed other manufacturers. It also has the capability to cut in two emulated tangential modes as well as drag knife mode (TM0) without needing to change blades (Fig. 2). The first tangential mode (TM1) lifts and turns the blade, just to the surface, at each line segment. The second tangential mode (TM2) lifts the blade only at the beginning and

end of each series of continuous line segments. The machine over-cuts a programmable distance (between 0 and 1 mm) each time the blade lifts when using TM1 or TM2. This cutting plotter is able to cut sharp angled features using TM1 and cut curved features using TM0, without changing the blade or the cutting origin. The FC5100A-75 can also cut material up to 1.1 mm thick with a force up to 300 g.

Various films were tested including thick and thin polymer films, hard and soft films, films with and without adhesives, thermal adhesive coated films and pressure sensitive adhesive coated films. We also tested thin metal films and filter membranes. Table I is a list of the materials tested and their properties. Materials without release liners, such as filter membranes and thermal laminates, were cut after temporarily applying them to a layer of application tape. The application tape in these cases functioned as a release liner.

III. THEORY

The smallest features that can be cut in a film depend on certain mechanical properties. The major factors that limit feature size are tension in the material, blade sharpness, cutting speed, and material properties such as Young's modulus and Poisson's ratio [29]–[31]. Others have studied the mechanics of slitting polymer films [30], [31] and show that the stress (σ_{xx} normal to the film's cross section is greatest near the blade's edge. σ_{xx} is resisted by the shear stress τ_{yx} at the interface of the film's adhesive and release liner (Fig. 3). When the total force in the x direction is greater than the yield shear stress $\tau_{yx-\text{max}}$ of the film, multiplied by the bottom surface area of the feature, the feature will slide relative to the release liner. This will occur at a critical feature width w_c assuming a constant σ_{xx} for a given cutting speed, material, blade shape, and blade sharpness.

TABLE I
MATERIALS AND OPTIMAL PLOTTER SETTINGS

Material Name	Maker	Part #	Material	Young's Modulus (MPa)	Poisson's Ratio	Adhesive	Material Thickness (μm)	Adhesive Thickness (μm)	Release liner	Cutting Mode	Blade angle	Force
Rubylith [®]	Ullano Corp.	RM3	Red emulsion	175	0.47	none	25	0	Poly-ester	TM0	45	5
Static Vinyl	unknown	unknown	Clear high static vinyl	6	0.49	none	190	0	AT	TM2 \pm 0.1mm	45	15
Clear Vinyl	3M	Scotchcal 220	Clear vinyl	125	0.49	acrylic	50	25	Kraft	TM0	45	9
Cast Vinyl	3M	Scotchcal 220	Cast white vinyl	108	0.49	PSA	50	25	Kraft	TM0	45	10
Calendered Vinyl	Gerber Sci.	Quantum 2000	Calendered vinyl	288	0.46	PSA	75	25	Kraft	TM0	45	12
Polyester	3M	9798R	White polyester	1932	0.39	PSA	51	19	Kraft	TM0	45	13
Green Sandblast Mask	Hartco, Inc.	315	Vinyl foam sandblast stencil	140	0.31	water based acrylic	300	60	Kraft	TM2 + 0.1mm	45	20
Tan Sandblast Mask	3M	520 series	Tan rubber sandblast stencil	6	0.49	unknown	1000	unknown	Poly-ester	Sharp angles: TM1 \pm 0.2 mm Smooth shapes: TM2 \pm 0.2 mm	60	25
Thermal Transfer	Gerber	Edgeheat	Thermal adhesive	44	0.45	thermal	0	25	Kraft	TM0	45	8
Thermal Laminate	Xerox	3 mil laminate	Clear Polyester	1175	0.40	thermal	15	61	AT	TM0	45	13
Thermal Laminate	GBC	5 mil HeatSeal	Clear Polyester	1048	0.40	thermal	76	51	AT	TM2 + 0.1mm	60	12,13,7
Thermal Laminate	GBC	10 mil HeatSeal	Clear Polyester	1390	0.40	thermal	178	76	AT	TM2 \pm 0.1mm	60	15,18,20, 22,24,10
Filter Paper	Milli-pore	Hardened	Nitro-cellulose	NM	NM	none	110	0	AT	TM0	45	3,5,7,7
Aluminum	3M	9792R	Aluminum	3148	0.35	PSA	39	30	Kraft	TM0	45	5,7,8

PSA = Pressure Sensitive Acrylate.

Kraft = Polyethylene coated, bleached Kraft paper with a silicon coating on one side.

AT = Application Tape.

TM0, TM1, and TM2 refer to the cutting modes discussed in Fig. 2.

NM = not measured

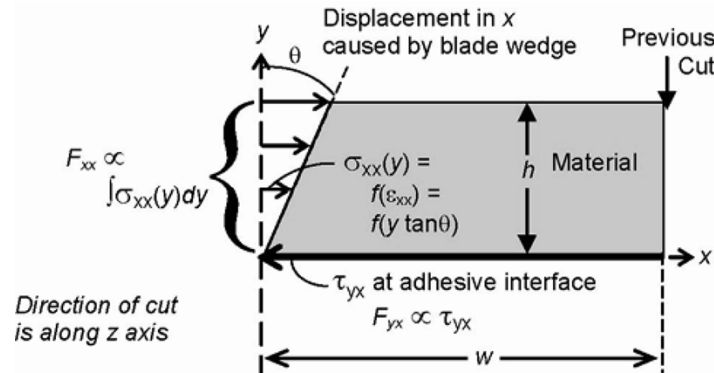


Fig. 3. Force diagram of a film's cross section. Normal stress σ_{xx} is resisted by the shear stress τ_{yx} . σ_{xx} is a function of the displacement $y \tan \theta$. The total normal force F_{xx} is resisted by the shear force F_{yx} at the adhesive interface.

The 2-D Hooke's law for isotropic material defines σ_{xx} as a function of the strain ε , the material's Young's modulus E , and its Poisson's ratio ν [32]

$$\sigma_{xx} = \frac{E}{(1 + \nu)(1 - 2\nu)} (\varepsilon_{xx}(1 - \nu) + \nu\varepsilon_{yy}). \quad (1)$$

$$\varepsilon_{yy} = -\varepsilon_{xx}/\nu.$$

ε_{xx} varies with y according to the blade's wedge angle (θ) and the width (w) of the previously cut feature. Thus

$$\varepsilon_{xx}(y) = -y \tan \theta / w, \quad (3)$$

$$\sigma_{xx}(y) = \frac{E\nu}{(1 + \nu)(1 - 2\nu)} \left(\frac{y \tan \theta}{w} \right). \quad (4)$$

The total force along x (F_{xx}), normal to the cross section of material being cut, is the integration of $\sigma_{xx}(y)$ along the height

of the material h , times the length of the blade L . The shear force resisting F_{xx} along the adhesive interface is F_{yx}

$$F_{xx} = L \frac{h^2 E \tan \theta \nu}{2w(1 + \nu)(1 - 2\nu)}. \quad (5)$$

$$F_{yx} = Lw\tau_{yx}. \quad (6)$$

As w decreases, τ_{yx} approaches $\tau_{yx-\max}$ until F_{xx} equals F_{yx} at the critical width w_c , which can be approximated as

$$w_c = \sqrt{\frac{h^2 E \tan \theta \nu}{2(1 + \nu)(1 - 2\nu)\tau_{yx-\max}}}. \quad (7)$$

Therefore, thinner, softer material, with low Poisson's ratio, and a high $\tau_{yx-\max}$ generally produce smaller features.

IV. METHOD

A. Plotter Settings

In order to achieve the highest resolution possible, the Graphtec FC5100A-75 was set at 10 μm addressable resolution with the slowest speed and acceleration. Test patterns and designs were drawn with 10 μm resolution in a CAD program and imported into Adobe Illustrator. The FC5100A-75 was controlled by a Graphtec plug-in application for Illustrator, called "Cutting Master." The channel test pattern (see Fig. 2) was used to determine the best machine settings that were material independent. Setting optimization was based on visual examination of the channel ends and circles with a 100 \times stereo microscope. A reticule was used to determine which settings achieved consistent channel widths, 90 $^\circ$ corners of rectangular features, and completely cut 500 μm diameter circles. The best material independent machine settings were as follows: Offset angle = 0, offset force = 4, and step pass = 0. Patterns were sorted before cutting, via an option in Cutting Master, to restrict media movement by layer so as to minimize material shift.

Next, the optimal material dependent settings were determined (see Table I). First, the square and triangle test pattern (see Fig. 2) were cut with a 45 $^\circ$ blade. The force settings were gradually increased until it was possible to remove the square without pulling up the triangle, thus indicating a complete cut. If corners tended to tear due to incomplete corner cuts, both tangential modes (TM1–TM2) were tested with a start and/or end over-cut of 100 μm (the smallest over-cut setting). Overcuts were useful on materials thicker than 200 μm . The channel test patterns (see Fig. 2) were used to compare TM1 and TM2 on materials that required overcuts. The optimal mode was determined by the smallest channel that was removable without breaking from the weeding tab. After mode selection, the same pattern was cut with the 60 $^\circ$ blade to determine the best blade for each material.

Small features were difficult to cut in harder materials such as polyester based films because the blade tips tended to break at sharp corners. In these cases, the sharp angle were cut with over-cuts using TM1. Alternatively, the patterns could be redrawn with rounded corners, or fillets. Another way to avoid breaking the tip when cutting hard thick materials was to cut

it multiple times with lower force settings without resetting the cutting origin, increasing the force after each pass.

B. Weeding

The cut film was weeded using a fine pair of tweezers and a 50 \times stereo microscope. Even though this was a bit tedious, dense patterns up to 100 cm^2 took only 15 min to weed. Isolated features like circles less than 250 μm or channels less than 100 μm were especially difficult to weed. Weeding tabs greater than 250 μm were attached to one or more ends of the smaller channels to avoid this difficulty. The smaller channels easily pulled up when the tabs were picked out with tweezers. The space left by the tabs can be used for fluidic ports or electronic leads.

C. Heat Lamination

A Xerox XRX-LM1910, 10" heat laminator with temperature control, was used to laminate thermal films to glass, plastic and other layers of thermal laminates. Laminating temperatures were set at $\sim 95^\circ\text{C}$ to melt thermal adhesive just enough to seal but not so high that the adhesive melted into the microchannels.

D. Characterization

After determining the best cutting method for each material, the long channels were measured at the start and the middle of the channels to determine accuracy and taper (narrowing of the channel due to blade and/or material movement) for positive and negative features (see Table II). Next, serpentine channels (see Fig. 2) were cut to determine minimum feature spacing. Measurements larger than 300 μm were done with a 100 \times microscope with 5 μm reticule markings. SEM images were analyzed with ImageJ, a free image analysis program from NIH (<http://rsb.info.nih.gov/ij/>), to measure features less than 300 μm . Film thickness was measured by a caliper ($\pm 10 \mu\text{m}$) or taken from the manufacturers' specifications.

E. Material Property Measurements

The Young's modulus E and yield shear strength $\tau_{yx-\max}$ for each material were measured by an Instron[®] 4443 universal materials testing machine. Stress vs. strain was measured on strips of film while stretching them at 10 mm/min without their release liners. The yield shear strength was found by measuring the peak force required to separate a film from its release liner and dividing it by the overlap area of the two layers. The film and release liner were pulled apart in a direction parallel to the plane of the film. Films were reinforced with a layer of calendered vinyl to minimize stretching before the yield shear strength was reached. Poisson's ratios were measured in the Hookean region [32].

V. RESULTS AND DISCUSSION

Table II shows each material's minimum feature size for various patterns. In general, the start of the channels deviated less than 10 μm from the drawn dimensions, which is within the addressable resolution of the plotter. There were some exceptions to this rule. For example, the large inaccuracies on the tan sand-blast and the two thickest thermal films may be because these were the only material the 60 $^\circ$ blade was used on. The shorter

TABLE II
MINIMUM FEATURE SIZES

Material	Total Material Thickness (μm)	Smallest Positive Channel Width (μm)				Smallest Negative Channel Width (μm)				Single Slice Width (μm)			Smallest Serpentine Channel Width and Spacing Dimensions (μm)		
		Drawn	Actual Start	Actual Middle	AR	Drawn	Actual Start	Actual Middle	AR	Top	Bottom	AR	Drawn	Average Channel	Average Spacing
Rubylith*	25	40	32	38	0.7	10	15	21	1.4	6	6	4	80	93 \pm 22	64 \pm 18
Static Vinyl	190	150	140	80	1.7	100	90	15	3.6	10	NM	19	200	162 \pm 42	262 \pm 64
Clear Vinyl	75	110	105	93	0.8	70	78	54	1.1	20	2	7	250	268 \pm 13	231 \pm 18
Cast Vinyl	75	100	102	76	0.8	80	43	17	2.5	19	3	7	180	180 \pm 34	177 \pm 16
Calendered Vinyl	100	80	47	43	2.3	70	53	29	2.5	32	2	6	120	99 \pm 11	111 \pm 36
Polyester	70	110	73	33	1.3	110	72	52	1.1	48	16	2	200	204 \pm 26	196 \pm 26
Green Sandblast	360	80	80	58	5.2	50	55	35	8.0	23	NM	16	200	147 \pm 71	239 \pm 29
Tan Sandblast	1000	500	540	460	2.0	200	185	150	6.0	40	14	37	500	450 \pm 117	463 \pm 49
Thermal Transfer	25	60	88 \pm 10	127 \pm 17	0.2	60	58 \pm 14	58 \pm 14	0.4	Re-seals	NM	NM	110	78 \pm 23	137 \pm 16
Laminate	76	70	72	58	1.2	60	57.96	40	1.6	16	1	9	120	122 \pm 27	105 \pm 29
Thermal Laminate	127	100	96	92	1.4	70	53	41	2.7	7	3	28	200	106 \pm 8	267 \pm 10
Thermal Laminate	254	300	339	294	0.8	250	248	248	1.0	95	10	5	400	291 \pm 40	460 \pm 10
Filter Paper	110	500	526	526	0.2	NM	NM	NM	NM	NM	NM	NM	500	519 \pm 52	526 \pm 50
Aluminum	69	250	288	278	0.3	250	247	238	0.4	40	14	3	500	129 \pm 91	485 \pm 135

AR – Aspect Ratio. This was calculated by dividing the material thickness by the average of the actual start and final channel dimensions.

NM – not measured

leading edge of the 60° blade, compared to the 45° blade, may reduce control of the blade as it swivels into position. The start of the positive channels in the aluminum and paper films were also off by more than 10 μm . These films tended to catch on the blade and tear before cutting, which may have affected the swivel of the blade as it started its cut into the channels. The smallest features of the calendered vinyl and white polyester films were inaccurate by more than 30 μm , the reasons of which are explained later.

Fig. 4 compares the actual start of the positive channels to the predicted w_c in (7). The material thickness without the adhesive was used to calculate w_c . The aluminum and paper films are not included in the trend line because they tended to catch on the blade and tear before cutting. The predicted values were not in perfect agreement with the measure results and were scaled by 0.04. This scaling factor accounts for constants not in the model, such as cutting speed and stresses at the leading edge of the blade. The discrepancies of the model (reduced $\chi^2 = 1.32$) may be due to other factors not accounted for, such as blade wear, material hardness, and friction. The model also assumes that stresses and strains remain in the Hookean region; however some materials permanently compressed under the blade. Crushed materials were wider at the tops of the channels than at the bottom as seen in the single slice channel dimensions. Despite the factors missing from the model, there is a correlation between minimum feature width and the ratio of material properties (E , ν , and $\tau_{yx-\max}$) described in (7). The correlation coefficient for Fig. 4 does indicate that the variance in the measured minimum width is attributed, at least in part, to the variance in the estimate of w_c ($P > 99\%$). Thus, in general, thinner, softer material, with low Poisson's ratio, and a high $\tau_{yx-\max}$ will produce smaller features.

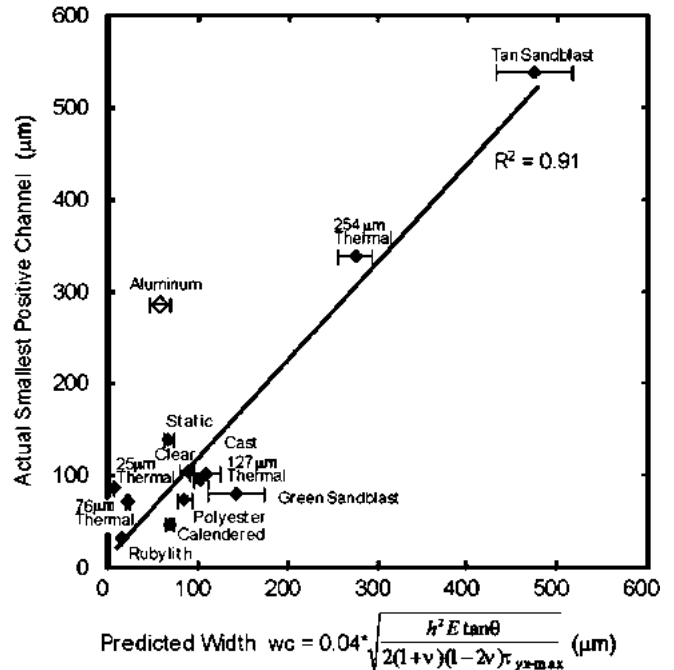


Fig. 4. Minimum channel width versus predicted width w_c . The 0.04 scaling factor accounts for constants not included in (7). Aluminum was not included in the trend line because it tended to catch on the blade and tear before cutting. Although some factors are missing from the model, there is a correlation ($P > 99\%$) between minimum feature width and the ratio of material properties (E , h , and $\tau_{yx-\max}$) used to estimate w_c .

The smallest features for both positive and negative channels tapered from the initial dimension to a smaller final dimension in the middle of the channel. Once tapered, channel width varied less than 2 μm (sidewall surface roughness was not measured). The exception to this was the thermal transfer film because the

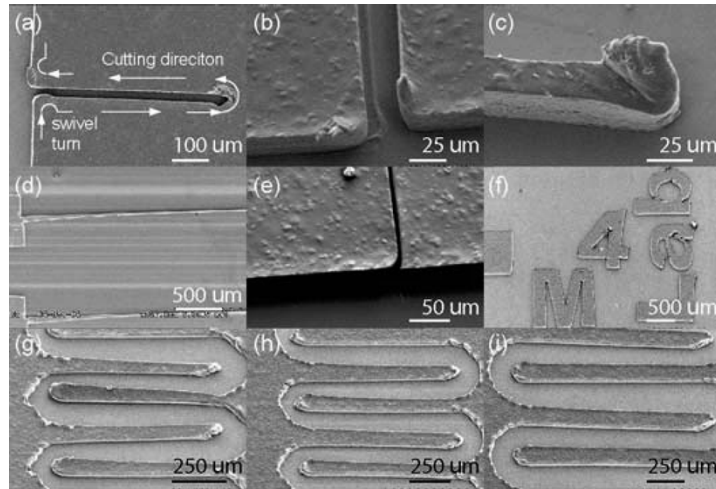


Fig. 5. Patterns cut in Rubylith®. (a) 21 μm channel (drawn 10 μm wide) without a fillet. (b) The same channel cut with a 50 μm fillet. (c) 32 μm positive structure (drawn 40 μm). (d) Tapering of a 50 and a 60 μm channel drawn without a fillet. (e) A single 6 μm slice. (f) Lab logo showing potential of positive patterns. Serpentine channels drawn at (g) 80 μm , (h) 100 μm , and (i) 140 μm width and spacing. Variability decreases to $\sim 10 \mu\text{m}$ for serpentine channels that were at least $2 \times$ greater than those recorded in Table II.

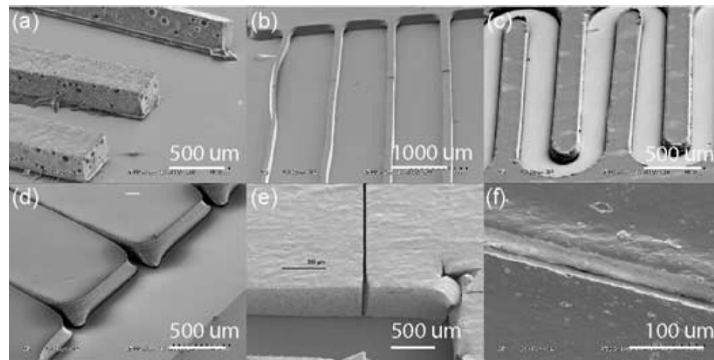


Fig. 6. Positive channels, negative channels, and serpentine channels in various films. (a) 100–80 μm features in 360 μm thick green sandblast. (b) 150–180 μm features in 190 μm thick static vinyl. (c) 250 μm channels in 75 μm thick clear vinyl. (d) 120–100 μm channels in 190 μm thick static vinyl. (e) 40 μm single slice in 1000 μm thick tan (rubber) sandblast mask. (f) single slice in 100 μm thick calendered vinyl.

adhesive melted into the channels. The distance from the start of the channel to the final tapered dimension varied for each material and channel width. It was observed that for the same material, the 60° blade caused the channels to taper sooner than the 45° blade. The calendered vinyl and white polyester films had relatively short taper lengths which made it difficult to measure the exact starting width of each channel. This may explain the deviations in channel dimensions from their drawn sizes for these films.

The taper can be explained from the derivation of w_c above (7). For dimensions less than w_c , the shear force F_{yx} (6) is less than the lateral force F_{xx} (5) causing the blade to move toward the first cut. Taper was much less prominent in single channels that were at least $2 \times$ greater than the smallest positive channel dimensions listed in Table II. In these cases, neither taper nor deviation from drawn dimension exceeded 10 μm , probably because F_{xx} doesn't exceed F_{yx} .

Rubylith® was the only material that had a positive taper. This was because the fillet into the smallest channels was less than the machine's minimum radius of curvature of 50 μm . The minimum radius of curvature can be seen in Fig. 5(a) where the

blade swiveled into a 90° turn without a fillet. The smallest channels on the calendered vinyl also had fillets less than 50 μm which may have contributed to its inaccuracy.

Table II only shows the minimum feature sizes for channels cut perpendicular to the material feed direction in the cutting plotter. Minimum features sizes for channels cut parallel to the material feed direction were about 10–20 μm greater. This was probably due to differences between the blade positioning and material feed motors on the cutting plotter.

The high variability of the serpentine channels occurred mostly at the turns and tapers in the channels. The variability decreases to about 10 μm for serpentine channels that were at least $2 \times$ greater than those recorded in Table II.

VI. EXAMPLE APPLICATIONS

With exception of the shadow mask and electroplated structures, the following microstructures were built without the use of a clean room. Fig. 5 shows the cutting characteristics of the Rubylith® material. Fig. 6–7 show examples of other materials tested.

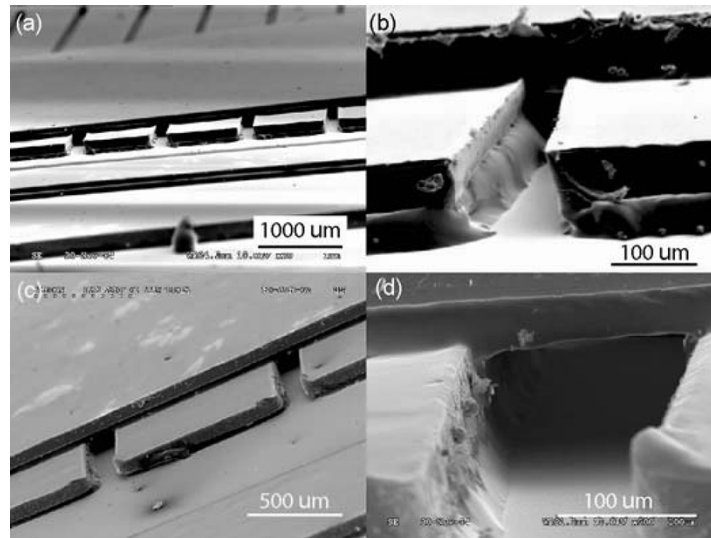


Fig. 7. Sealed channels. (a, b) The adhesive and polyester layers can be distinguished in channels cut in 127 μm thick thermal laminate. Since the channels were cut from the adhesive side, they are slightly narrower at the top than they are at the bottom. (c, d) Sealed channels in 75 μm thick clear adhesive vinyl.

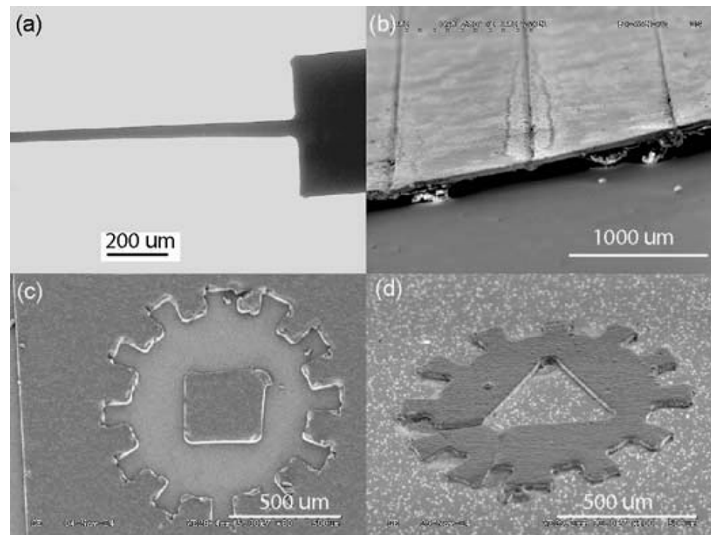


Fig. 8. (a) Silicon traces sputtered onto a glass slide using Rubylith® as a shadow mask. (b) Copper channels electroplated using Rubylith® as a sacrificial layer. The channel walls were destroyed during handling of the sample. (c) A negative 1 mm diameter gear with 100 μm teeth patterned in Rubylith®. (d) A positive gear electroplated with Rubylith® as a mask.

A. Shadow Mask

Rubylith® is normally used as a photomask for screen-printing, although it has also been used as a photomask in IC applications (www.ulano.com). It consists of a UV opaque emulsion without adhesive on a clear polyester backing. In order to use Rubylith® as a shadow mask, cut patterns were peeled off the release liner using application tape and then transferred to glass slides (see Fig. 1). The application tape was wetted with a small amount of water to reduce its adhesion to the Rubylith® and then peeled away using the technique described in Fig. 1. The Rubylith® stuck to the glass by electrostatic interaction.

Glass slides with patterns cut in Rubylith® were then placed in a Denton Discovery 18 sputter system (100 W RF power, Ar flow of 50 sccm at 4.8 mTorr) for 30 minutes, to deposit a 375 nm layer of silicon. The Rubylith® was then peeled away,

leaving narrow channel traces that started at 55 μm and tapered down to 28 μm [see Fig. 8(a)].

B. Electroplating

Electroplated microchannels were created using Rubylith® as a sacrificial layer. Cut channels were transferred to a clean glass slide using the same method as described for shadow masking. Channel openings were covered with kapton tape and then the slide was placed in the sputter system (same system and settings as mentioned above). A 20 nm thick titanium seed layer (1 min sputtering time) was sputtered onto the slide followed by a 200 nm layer of gold (7 min sputtering time). The kapton tape was then removed and the slide was placed in a copper sulfate solution (100 g CuSO_4 : 25 ml H_2SO_4 : 450 ml DI H_2O). A 20 mA/cm^2 current density was applied for 50 min, forming an 18 μm copper deposition. The sacrificial Rubylith® was dissolved

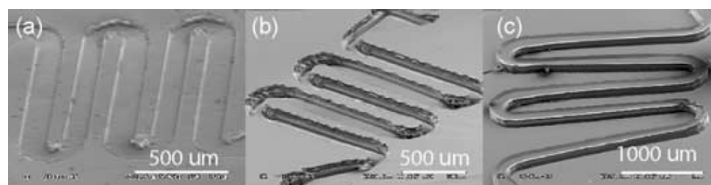


Fig. 9. PDMS patterns molded on xurographically cut (a) Rubylith® and (b) 127 μm thick thermal laminate. (c) A positive 250 μm serpentine channel in 127 μm thick laminate used for molding PDMS features similar to (b).

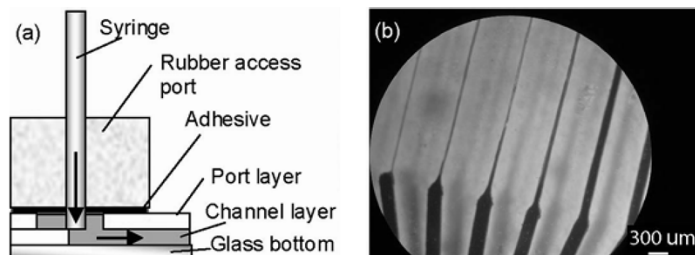


Fig. 10. (a) Rubber access ports made from the 1 mm thick sandblast masking material. (b) Flow in channels ranging from a single slice to 250 μm in 127 μm thick thermal laminate. Similar channels were fabricated in clear vinyl adhesive and static vinyl.

in acetone and rinsed with methanol and DI water, leaving the hollow electroplated channels.

Stand alone structures were also electroplated using a negative Rubylith® pattern. The pattern was transferred to a gold coated glass slide and the slide was then placed in the same copper solution as the channels mentioned above. Fig. 8 shows the electroplated channels and an electroplated gear.

C. Micromolding in PDMS

PDMS was molded on positive microstructures cut in Rubylith® and thermal laminate films (see Fig. 9). The Rubylith® patterns were left on the polyester release liner and the thermal films were laminated to glass cover slides. PDMS prepolymer was mixed with a curing agent (SYLGARD 184, Dow Corning, Midland, MI) at a 10:1 weight ratio and then poured over the Rubylith® and laminate structures [2]. The PDMS mixture was degassed at ~ 100 mtorr for 10 min to remove air bubbles. The samples were cured at 80 $^{\circ}\text{C}$ for 40 min. Higher temperatures cause the thermal glue on the laminate film to melt. The cured PDMS was then peeled away from the molds. Thermal laminate micromolds were successfully reused for recasting PDMS; however mold integrity after repeated use was not investigated. The Rubylith® micromold was also reusable, but only for features greater than ~ 100 μm . The smaller features tended to peel off the release liner with the PDMS. Features that stuck to the PDMS were rinsed off in acetone.

D. Laminated Microfluidic Structures and Ports

Fig. 10 shows fluid flow in 2-D channels cut in 127 μm thick thermal laminate film and sealed with the same material to a glass slide. Channels ranged from a single slice to 250 μm wide. The top layer sealing the channels had holes for port access. These holes were covered with a small piece of 1 mm thick sandblast mask material (~ 4 mm diameter) that had a needle hole poked through its center [see Fig. 10(a)]. A flat end 25 gauge syringe was inserted into the needle hole so that the sandblast material sealed around the syringe. Blue dye was then injected

into the channels. The maximum pressure for the rubber access ports is limited but can be improved with better adhesive backing. Similar channels were fabricated in clear vinyl adhesive and static vinyl. The static vinyl had to be clamped down to prevent leaking.

A 3-D microfluidic structure was cut in 127 μm thick thermal laminate film, following an example made in PDMS by Anderson *et al.* [8] which consists of a coiled channel surrounding a straight channel. Coupling holes, access ports, and alignment holes were also cut in the pattern. Because there were not any free standing features, the channels and holes were weeded by blowing them out with an air nozzle after peeling the cut pattern from the release liner (application tape). The coupling holes, which connected channels across layers, were relatively large (~ 300 μm) because of the difficulty of cutting and weeding smaller holes. Fig. 11 shows how each layer was aligned to the bottom layers by using two glass capillary tubes as alignment pins in the alignment holes. After alignment, each layer was taped to the previous layer, the glass tubes were removed, and then the taped layers were sent through the heat laminator, top side down to prevent the thermal adhesive from re flowing into the channel. Alignment within 60 μm was achieved using this method. The channels were designed to be 100 and 200 μm thick. The 100 μm straight channel narrowed to about 50 μm because of tapering. The entire seven-layer structure took less than 30 min to build.

VII. CONCLUSION

Xurography functions as a truly inexpensive and rapid prototyping method for microstructure fabrication. It can create microstructures in less than 30 min without photolithographic processes or chemicals. Laboratories without access to clean room microfabrication facilities can quickly design, build, and test first stage microfluidic device prototypes for a variety of applications, such as biochemical sensors. After feasibility and design are tested using xurographic fabrication, the devices can be built using techniques that are conducive for high throughput, such as injection molding.

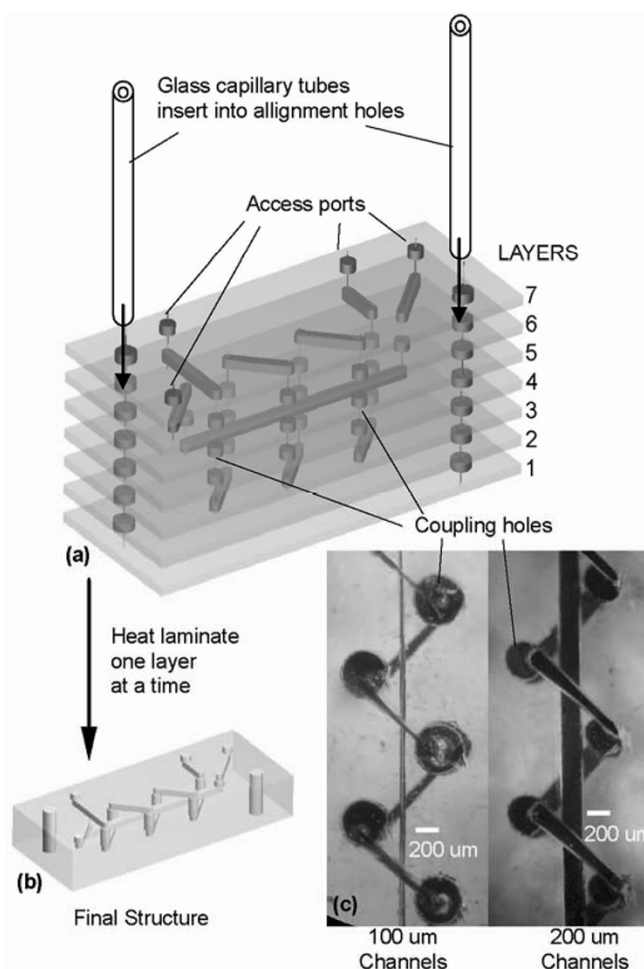


Fig. 11. (a) Layered structures to build a 3-D coiled channel surrounding a straight channel in 127 μm thick thermal laminate. Each layer consisted of coupling holes, access ports, and alignment holes. (b) The final structure. (c) Dye flowing in channels drawn at 100 and 200 μm 3-D channels.

Although xurography does not have as high of a resolution as standard lithographic techniques, the accuracy of this method is within 10 μm of drawn dimensions and feature variability is less than 2 μm . When higher resolution or materials that cannot be cut by a blade are required, such as semi-conductor based sensors, xurographically cut channels can be laminated on top to function as tertiary fluid connections. Pressure sensitive films also make it possible to safely seal channels or wells filled with thermally labile reagents for biosensor applications.

The xurographic method described here can be further studied for machine and material optimization. Higher addressable resolution of the plotter, down to the width of the blade edge, can improve accuracy. Smaller holes could be fabricated by operating a heated pouncing needle in tandem with the blade. According to (7), a smaller Young's modulus E and larger yield shear strength $\tau_{yx-\text{max}}$ can also improve feature size. The Young's modulus can be reduced by heating the blade to the films melting temperature. The heated blade could also anneal the channel to make the walls smoother, reducing surface tension (a significant factor in microfluidics) within the channel. An increase in $\tau_{yx-\text{max}}$ would potentially improve feature size, but would make it difficult to weed. A possible solution is to use a UV degradable adhesive on the release liner. $\tau_{yx-\text{max}}$ would be high while cutting, holding smaller features

in place, and reduced after exposure to UV. This could work well for nonadhesive films.

Specialty films could be created for specific applications. Passive valves in Teflon[®] cut using xurography would be less expensive than laser ablation [13], [14]. Xurographically cut UV curable or UV degradable polymer films could be used to build up structures or function as sacrificial layers in PDMS, SU-8, or metal structures. Some materials could also be fabricated on a release liner with a slight internal tension so as to create specific channel widths with a single slice.

Xurographic prototyping is less precise than other fabrication methods but is a useful and inexpensive research tool. The time and prototyping costs saved will allow researchers to focus on the device development before moving on to more expensive fabrication techniques.

ACKNOWLEDGMENT

D. B. Bartholomeusz would like to thank B. Baker of the University of Utah's Micro-fabrication Facility for helping with the electroplating and suggestions for potential applications.

REFERENCES

- [1] D. R. Reyes, D. Iossifidis, P. A. Aurox, and A. Manz, "Micro total analysis systems. 1. Introduction, theory, and technology," *Anal. Chem.*, vol. 74, pp. 2623–2636, 2002.

- [2] D. C. Duffy, J. C. McDonald, O. J. A. Schueller, and G. M. Whitesides, "Rapid prototyping of microfluidic systems in poly(dimethylsiloxane)," *Anal. Chem.*, vol. 70, pp. 4974–4984, 1998.
- [3] Y. Xia and G. M. Whitesides, "Soft lithography," *Annu. Rev. Mater. Sci.*, vol. 28, pp. 153–184, 1998.
- [4] A. Folch, A. Ayon, O. Hurtado, M. A. Schmidt, and A. Toner, "Molding of deep polydimethylsiloxane microstructures for microfluidics and biological applications," *J. Biomech. Eng.*, vol. 121, pp. 28–34, 1999.
- [5] J. C. McDonald, D. C. Duffy, J. R. Anderson, D. T. Chiu, H. Wu, O. J. Schueller, and G. M. Whitesides, "Fabrication of microfluidic systems in poly(dimethylsiloxane)," *Electrophoresis*, vol. 21, pp. 27–40, 2000.
- [6] B. H. Jo, L. M. Van Lerberghe, K. M. Motsegood, and D. J. Beebe, "Three-Dimensional microchannel fabrication in polydimethylsiloxane (PDMS) elastomer," *J. Microelectromech. Syst.*, vol. 9, pp. 76–81, 2000.
- [7] T. Deng, H. Wu, S. T. Brittain, and G. M. Whitesides, "Prototyping of masks, masters, and stamps/molds for soft lithography using an office printer and photographic reduction," *Anal. Chem.*, vol. 72, pp. 3176–3180, 2000.
- [8] J. R. Anderson, D. T. Chiu, R. J. Jackman, O. Cherniavskaya, J. C. McDonald, H. Wu, S. H. Whitesides, and G. M. Whitesides, "Fabrication of topologically complex three-dimensional microfluidic systems in PDMS by rapid prototyping," *Anal. Chem.*, vol. 72, pp. 3158–3164, 2000.
- [9] T. Thorsen, S. J. Maerkl, and S. R. Quake, "Microfluidic large-scale integration," *Science*, vol. 298, pp. 580–584, 2002.
- [10] M. Brivio, R. H. Fokkens, W. Verboom, D. N. Reinhoudt, N. R. Tas, M. Goedbloed, and A. V. D. Berg, "Integrated microfluidic system enabling (bio)chemical reactions with on-line MALDI-TOF mass spectrometry," *Anal. Chem.*, vol. 74, pp. 3972–3976, 2002.
- [11] B. H. Weigl, R. Bardell, T. Schulte, and C. Williams, "Passive microfluidics—Ultra-low-cost plastic disposable lab-on-a-chips," presented at the Micro Total Analysis Systems 2000, Dordrecht, The Netherlands, 2000.
- [12] B. H. Weigl, R. Bardell, T. Schulte, F. Battrell, and J. Hayenga, "Design and rapid prototyping of thin-film laminate-based microfluidic devices," *Biomed. Microdev.*, vol. 3, pp. 267–274, 2001.
- [13] M. R. McNeely, M. K. Sputea, N. A. Tusneem, and A. R. Oliphant, "Hydrophobic microfluidics," in *Proc. SPIE Microfluidic Devices and Systems II*, vol. 3877, 1999, pp. 210–220.
- [14] M. R. McNeely, M. K. Sputea, N. A. Tusneem, A. R. Oliphant, and A. J. A. Lab, "Sample processing with hydrophobic microfluidics," *J. Assoc. Lab. Automat.*, vol. 4, pp. 30–33, 1999.
- [15] A. Bertsch, S. Jiguet, and P. Renaud, "Microfabrication of ceramic components by microstereolithography," *J. Micromech. Microeng.*, vol. 14, pp. 197–203, 2004.
- [16] G. S. Fiorini, R. M. Lorenz, J. S. Kuo, and D. T. Chiu, "Rapid prototyping of thermoset polyester microfluidic devices," *Anal. Chem.*, vol. 76, pp. 4697–4704, 2004.
- [17] C. R. Friedrich and M. J. Vasile, "Development of the micromilling process for high-aspect ratio microstructures," *J. Microelectromech. Syst.*, vol. 5, pp. 33–38, 1996.
- [18] H. Lorenz, M. Despont, N. Fahrni, N. LaBianca, P. Renaud, and P. Vettiger, "SU-8: A low-cost negative resist for mems," *J. Micromech. Microeng.*, vol. 7, pp. 121–124, 1997.
- [19] J. H. Klein-Wiele and P. Simon, "Sub-Micron sized periodic 3d surface structures fabricated by femtosecond UV laser pulses," in *Proc. SPIE Fourth International Symposium on Laser Precision Microfabrication*, vol. 5063, 2003, pp. 445–448.
- [20] M. J. Madou, *Fundamentals of Microfabrication: The Science of Miniaturization*, 2nd ed. Boca Raton, FL: CRC, 2002.
- [21] A. Rasmussen, M. Gaitan, L. E. Locascio, and M. E. Zaghoul, "Fabrication techniques to realize CMOS-compatible microfluidic microchannels," *J. Microelectromech. Syst.*, vol. 10, pp. 286–297, 2001.
- [22] M. Farsari, F. Claret-Tournier, S. Huang, C. R. Chatwin, D. M. Budget, P. M. Birch, R. C. D. Young, and J. D. Richardson, "A novel high-accuracy microstereolithography method employing an adaptive electro-optic mask," *J. Mater. Processing Tech.*, vol. 107, pp. 167–172, 2000.
- [23] N. T. Nguyen and S. T. Wereley, *Fundamentals and Applications of Microfluidics*. Norwood, MA: Artech House, 2002.
- [24] G. T. A. Kovacs, *Micromachined Transducers Sourcebook*. New York: The McGraw-Hill, 1998.
- [25] D. C. Duffy, H. L. Gillis, J. Lin, N. F. Sheppard Jr., and G. J. Kellogg, "Microfabricated centrifugal microfluidic systems: Characterization and multiple enzymatic assays," *Anal. Chem.*, vol. 71, pp. 4669–4678, 1999.
- [26] M. Griffiths, "Rapid prototyping options shrink development costs," *Modern Plastics*, vol. 70, pp. 45–47, 1993.
- [27] Y. Guoxing, D. Yucheng, L. Dichen, and T. Yiping, "A low cost cutter-based paper lamination rapid prototyping system," *International J. of Machine Tools & Manufacture*, vol. 43, pp. 1079–1086, 2003.
- [28] G. Yu, Y. Ding, and D. Li, "Cutting mechanism of a cutter-based paper lamination rapid prototyping system," *Chinese J. of Mech. Eng.*, vol. 40, pp. 44–49, 2004.
- [29] R. R. Meehan, J. Kumar, M. Earl, E. Svenson, and S. J. Burns, "The role of blade sharpness in cutting instabilities of polyethylene terephthalate," *J. Mater. Sci.*, vol. 18, pp. 93–95, 1999.
- [30] C. Arcona and T. A. Dow, "The role of knife sharpness in slitting of plastic films," *J. Mater. Sci.*, vol. 31, pp. 1327–1334, 1996.
- [31] R. R. Meehan and S. J. Burns, "Mechanics of slitting and cutting webs," *Exper. Mech.*, vol. 38, pp. 103–109, 1998.
- [32] D. S. Chandrasekharaiah and L. Debnath, *Continuum Mechanics*. New York: Academic, 1994, pp. 366–375.



Daniel A. Bartholomeusz received the B.S. degree in bioengineering (ABET) from the University of California at San Diego, in 1999. In 2002, he received the University of Utah Graduate Research Fellowship Award for his current Ph.D. dissertation research in developing a bioluminescence-based biosensor for multiple analytes.

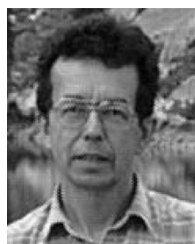
While working on his undergraduate degree, he was a Research and Development Intern at Aurora Biosciences, La Jolla, CA. There, he worked on picoliter sample delivery systems for drug discovery.



Ronald W. Boutté is currently working towards the B.S. degree in electrical engineering at the University of Utah, Salt Lake City.

From 1998 to 2002, he was President of DLUX Communication, Inc., which specialized in the construction of hybrid fiber/coax network systems. He participated in the mathematics and science outreach as an exhibit coordinator for the Utah Science Center from 2002 to 2004. His research interests are in the clinical applications of microfluidic systems for bioluminescent assays and the development of rapid-

prototyping systems for electrodes in electrochemical sensors and MEM's devices.



Joseph D. Andrade received the B.S. degree in materials science from San Jose State University, CA, in 1965. He received the Ph.D. degree in metallurgy and materials science from the University of Denver, CO, in 1969.

He joined the University of Utah in 1969, working with Professor W. Kolff. Since then, his service at the University of Utah has included Chairman of the Department of Bioengineering (1978–1981, 1988–1991, and 1998–2000 as Co-Chair), Dean of the College of Engineering (July 1983–September 1987), Interim Chairman of the Department of Pharmaceutics (1998), Co-Director for the Center for Science Education and Outreach (1991–Present). He is also Director of the Utah Science Center (www.utahsciencecenter.org). His published books include: *Medical and Biological Engineering in the Future of Health Care* (Salt Lake City, Utah: University of Utah Press, 1994), *Surface and Interfacial Aspects of Biomedical Polymers*, Vol. 1, (New York: Plenum, 1985), and *Hydrogels for Medical and Related Applications* (Amer. Chem. Soc. Symp. Series no. 31, 1976). His current research activities are focused on reducing health care costs through patient empowerment. His group is developing sensitive, inexpensive biochemical sensors using bioluminescence-based technology.

Dr. Andrade is a member of the following societies: American Association for Advancement of Science (AAAS), Founding Fellow of the American Institute for Medical and Biological Engineering (AIMBE), American Association for Clinical Chemistry (AACC), American Association of Physics Teachers (AAPT), American Chemical Society (ACS), American Institute of Biological Sciences (AIBS), American Physical Society (APS), Biomaterials Society, Controlled Release Society (CRS), National Association of Biology Teachers (NABT), National Science Teachers Association (NSTA), and the New York Academy of Sciences (NYAS).

Optical enhanced luminescent measurements and sequential reagent mixing on a centrifugal microfluidic device for multi-analyte point-of-care applications

Daniel A. Bartholomeusz^{*a}, Rupert H. Davies^b, Joseph D. Andrade^a

^aDept. of Bioengineering, University of Utah, 50 S. Central Campus Drive, 2480 MEB,
Salt Lake City, UT USA 84112-9202

^bDept. of Bioengineering, University of Washington, 411 Bagley Hall, Box 351721,
Seattle, WA USA 98195-1721

ABSTRACT

A centrifugal-based microfluidic device¹ was built with lyophilized bioluminescent reagents for measuring multiple metabolites from a sample of less than 15 μL . Microfluidic channels, reaction wells, and valves were cut in adhesive vinyl film using a knife plotter with features down to 30 μm and transferred to metalized polycarbonate compact disks (CDs). The fabrication method was simple enough to test over 100 prototypes within a few months. It also allowed enzymes to be packaged in microchannels without exposure to heat or chemicals. The valves were rendered hydrophobic using liquid phase deposition. Microchannels were patterned using soft lithography to make them hydrophilic. Reagents and calibration standards were deposited and lyophilized in different wells before being covered with another adhesive film. Sample delivery was controlled by a modified CD ROM. The CD was capable of distributing 200 nL sample aliquots to 36 channels, each with a different set of reagents that mixed with the sample before initiating the luminescent reactions. Reflection of light from the metalized layer and lens configuration allowed for 20% of the available light to be collected from each channel. ATP was detected down to 0.1 μM . Creatinine, glucose, and galactose were also measured in micro and milliMolar ranges. Other optical-based analytical assays can easily be incorporated into the device design. The minimal sample size needed and expandability of the device make it easier to simultaneously measure a variety of clinically relevant analytes in point-of-care settings.

Keywords: Bioluminescence, centrifugal devices, microfluidics, point-of-care, rapid-prototyping

1. INTRODUCTION

1.1. Point-of-Care

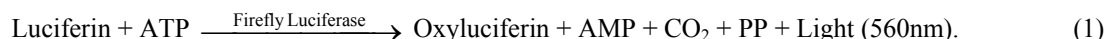
During the past 10 years, some in vitro diagnostic (IVD) testing has moved from centralized labs to point of care testing. The point-of-care (POC) is where treatment decisions are made and includes emergency rooms, battlefields, outpatient clinics, nursing homes, patients' homes, or hospital bedside. POC testing is mostly used in applications that require frequent testing, such as diabetes, or for tests that need to be done quickly, such as in emergency rooms. POC sensors are being developed around the need to measure common analytes, which include blood gases, coagulation, and general chemistry, and immunoassays for drugs and proteins to provide physicians and caregivers with quantitative information to diagnose, triage, and treat patients².

Effective management of some pathologies require regular, routine clinical chemistry measurements of low molecular weight biochemicals important to metabolism. A well-known example is glucose measurements necessary for the management of diabetes. Other diseases such as the inborn metabolic diseases phenylketonuria (PKU)³ and galactosemia⁴ also need regular monitoring of relevant analytes. POC sensors for measuring multiple low molecular weight metabolites would help determine multi-parametric profiles of different pathologies in clinical diagnostics and research.

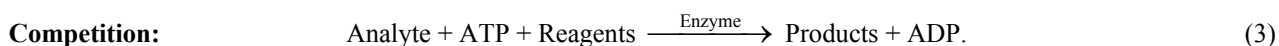
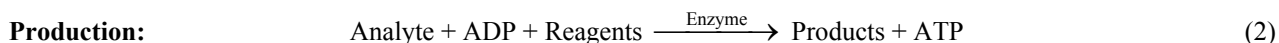
^{*} d.bartholomeusz@gmail.com

Luminescence-based detection is a highly sensitive and specific analytical method that is starting to be used more frequently in IVD laboratory analyzers, but has not been readily implemented in POC devices². Luminescence-based assays can have a detection range of five or more orders of magnitude without dilution or concentration of the sample fluid⁵. Luminescent reactions have inherently low background noise that can be 100 to 1,000 time less than that which can come from emission sources in fluorescence based measurements⁵ and can have up to 90% quantum efficiencies⁶. In the last 20 years, the detection limit of luminescence-based methods has improved from 10⁻¹⁴ moles (10 femtomoles) to 10⁻¹⁸ moles (1 attomole) using reasonably priced reagents and luminometers.

Bioluminescent reactions, which are luminescent reactions catalyzed by enzymes, have the potential to measure a wide range of low molecular weight metabolites. The firefly luciferase (FFL) reaction below is a common bioluminescent reaction involving Adenosine Triphosphate (ATP):



Metabolites can be measured by coupling the appropriate enzyme reaction(s) to an ATP bioluminescent reaction and measuring the light output. The specificity of the luminescence-based analysis is determined by the selectivity of a coupling reaction. Analytes of interest are measured by coupling them to enzymatic reactions that produce or consume ATP as follows:



Numerous metabolites can be measured using the ATP platform luminescent reaction (Equation 1) since many metabolites in the body are within one or two enzymatic reactions from ATP⁷. Even more metabolites can be measured by using reactions that produce or consume nicotinamide adenine dinucleotide (NADH) or H₂O₂. These reactions can be coupled to a bioluminescent platform consuming NADH through an oxidoreductase and bacterial luciferase reaction, or a chemiluminescent platform consuming H₂O₂ through a peroxidase reaction. Details of these platform reactions are discussed by Andrade *et al.*^{7, 8}. These platforms have already been used to measure metabolites in solution, human blood (serum & plasma), and urine.

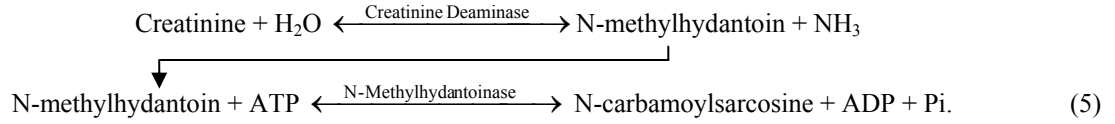
The changes in light intensity reflect stoichiometrically proportional changes in concentration of the platform molecule (ATP). The light intensity changes are proportional to the metabolite of interest. Equation 2 represents a production reaction, which feeds into one of the platform reactions (Equations 1). Higher concentrations of analyte produce more ATP and thus more photons (or photons per unit time) in production reactions. Competition reactions (Equation 3) consume more ATP, thus producing less intense signals as the concentration of the analyte increase.

Although bioluminescence-based analysis is well known and has been used regularly in research for sensitive reactions, it has not been widely applied to POC or routine clinical analysis due to issues associated with the enzymes. Luciferases have a reputation for being somewhat labile, unstable, and difficult to utilize, with precise and somewhat sophisticated protocols. However, there have been recent advances in enzyme stabilization techniques and highly active, thermally stable mutant luciferases that have become more available⁶, allowing bioluminescent detection assays to be prepared and stabilized with relatively straightforward protocols. Luciferases tend to be expensive, however the sensitivity of bioluminescence assays does not require large volumes for measuring microMolar analyte concentrations. Microfabrication and ink-jet dispensing make it possible to dispense small amount of enzymes, reducing the cost per test.

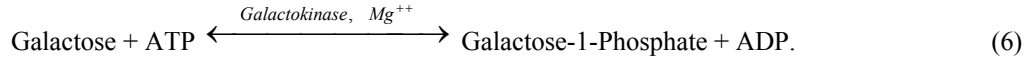
Through microfabrication and ink-jet dispensing, a bioluminescence based sensor capable of measuring multiple low molecular weight metabolites can be built. Different assay reagents can be deposited and lyophilized in separate reaction wells. Microfluidic structures can deliver sample aliquots to each well, whereupon the reagents rehydrate and the luminescent reactions begin. In addition to the ATP platform reaction, creatinine, galactose, and glucose assays were tested on a centrifugal based sample delivery system, or “ChemCD,” as described below.

1.2.1. Assays tested

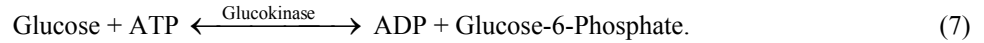
Serum creatinine measurements are used to assess kidney function and glomerular filtration rate⁶. Normal adult serum creatinine levels range from 50 to 100 μM . Since creatine concentration is relatively constant, the measurement of creatine in urine is used to allow for correction of urine dilution when measuring other analytes in urine. Creatine can be measured by coupling a two stage reaction, involving creatinine deaminase and N-methylhydantoinase, which competes for ATP in reaction (1):



Galactose measurements are used in the management of galactosemia. Normal serum galactose concentration in newborns is 0-44 μM , while galactosemics can have galactose concentrations in the millimolar range^{6, 9}. Galactose can be measured by competing for ATP in reaction (1) through the galactokinase reaction



Glucose is a frequently measured analyte and is commonly measured to help diabetics monitor and manage their blood glucose levels through diet and insulin injections. Glucose concentrations in blood can range from 3 to 6 mM in normal patients and 5 to 20 mM in diabetics. Glucokinase competes for ATP in reaction (1) as seen here:



1.3. Centrifugal devices

Simultaneous and quantitative measurements of multiple analytes through bioluminescence-based assays requires separation of sample aliquots. Since luminescent reactions involve cofactors that cannot be immobilized, reaction wells must be isolated, even if the enzymes are immobilized. If there was more than one reaction well in a channel, unbound reagents would flow from one well to another, causing crosstalk. Variations in sample volume could change the amount of analyte available to react as well as final enzyme concentrations after rehydration, thus affecting the luminescence.

Centrifugal pumping is an ideal sample delivery method for a bioluminescence-based POC device. It uses centrifugal force to move fluids radially outward from the center of a disk with fluidic channels. Centrifugal pumping is also capable of valving, decanting, calibration, mixing, metering, sample splitting, separation, and capillarity without sensitivity to bubbles, ions, or type of fluid^{1, 10}. Microfabricated centrifugal devices have been used in a variety of commercial and research applications¹¹. An extensive review of the principles of centrifugal pumping, fluid control, and applications was done by Zoval and Madou¹. Only a few details are presented here.

Passive valves, including hydrophobic and capillary valves, are commonly used in centrifugal devices^{1, 10} to meter, or aliquot, specific sample volumes for downstream reactions or other sensing functions¹. This is done by filling liquid metering reservoirs through common distribution channels at a low rotation rate (Fig. 1a). The fluid stops at the passive valve barrier and the excess fluid leaves the distribution chamber as the device continues to spin, leaving a metered volume (Fig. 1b). This sample volume then passes the barrier by increasing the spin speed ω until the centrifugal pressure P_C exceeds the valve's burst pressure P_V (Fig. 1c).

The effectiveness of hydrophobic and capillary valves, i.e. the magnitude of P_V , depends on the surface tension and contact angle of the fluid involved. Low surface tension fluids, including biological fluids, tend to have low contact angles, decreasing the maximum burst valve pressure for a given channel. Plasma's surface tension ranges from 25 – 55 dynes/cm ($\sigma_{\text{water}} \sim 73$ dynes/cm)¹² because proteins are present in high concentrations (> 1 mg/mL)¹³ and act as a surfactant.

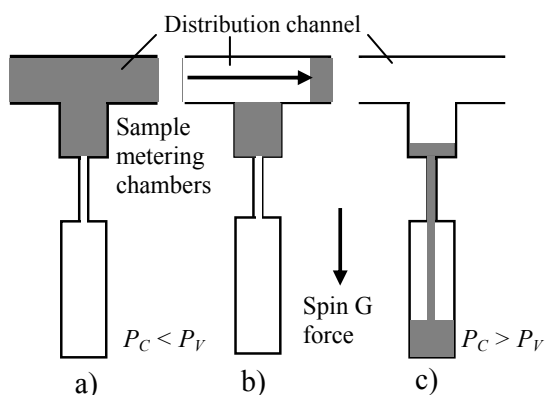


Figure 1: Sample metering with a passive valve.
Adapted from Zoval *et al.*¹

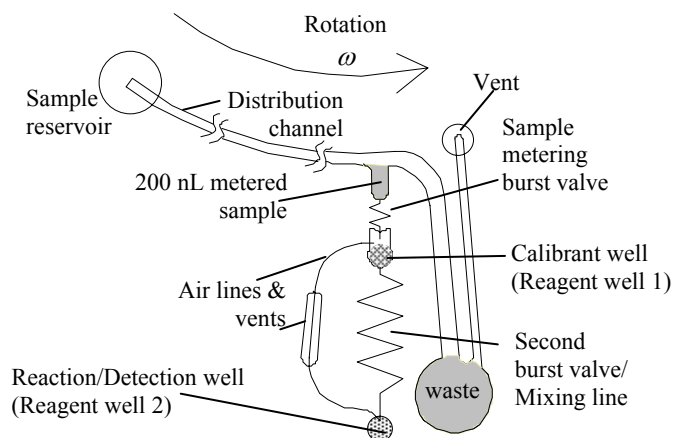


Figure 2: Sample metering from a distribution channel using zigzag burst valves followed by sequential mixing of lyophilized reagents.

2. METHODOLOGY

Zigzag shaped hydrophobic burst valves were built and tested on a compact disk (CD) shaped device to meter multiple aliquots of 200 nL samples into separate reaction channels (Fig. 2 & 3). The sample is delivered from a reservoir and pumped through a distribution channel to fill multiple metering chambers. Each channel had two wells, wherein reagents were deposited and lyophilized. After distributing the sample aliquots to each channel, the spin speed was increased to rehydrate and mix with the reagents. The bioluminescent reactions started as the sample, mixed with the reagents in the first well, entered into the 2nd reagent well/reaction well. The luminescent signal from each well was recorded as the CD rotated over a photomultiplier tube (PMT).

2.1. Fabrication

Prototypes were built using xurography, which is a rapid prototyping method that uses a knife plotter to cut microfluidic structures in adhesive films¹⁴. This prototyping method was fast and inexpensive enough to allow the device to go through over 100 design iterations within a few months, until the final design in Fig. 3 was achieved. To summarize, a Graphtec FC5100A-75 knife plotter (Graphtec, Irvine, CA) was used to cut channel and cover layers in adhesive backed films, which were then transferred to a CD substrate (Fig. 3). First, channels, valves, and wells were cut in 100 μm thick QuantumTM 2000 calendared vinyl film (Gerber Scientific, South Windsor, CT). The channels and wells were removed, or weeded, and transferred to metalized polycarbonate CDs using an alignment jig described below. The channel layer was then modified to create hydrophobic valves and hydrophilic channels and wells (also described below). The reagents were deposited in the wells and then lyophilized. Finally, the channels were covered with a 75 μm thick Scotchcal 220 clear adhesive vinyl (3M, St. Paul, MN) with air holes cut in it using the knife plotter.

2.1.1. Alignment

The channel and cover layers were aligned onto the CD using the alignment marks seen in Fig. 3 and 4. After weeding the channels and wells, the pattern was transferred to a clear application tape. With the pattern sticky side up on the application tape, the tips of the guide pins were manually aligned to the corner of the alignment marks (Fig. 4a). A 3/8" thick acrylic frame was then placed on the application tape (Fig. 4a,b). The outside corners of the alignment marks fit on the inside corners of the frame. The guide pins helped align the frame as it was being placed on the pattern. The CD was secured onto a 1/4" thick acrylic square that fit exactly inside the frame. The CD was held in position on the square by a 120 mm circle that was cut in 180 μm thick acrylic adhesive film and aligned on the square. The frame was then turned over (Fig. 4c) and placed over the square, holding the application tape with the pattern about 2 mm above the CD. The pattern was then pressed onto the CD using a plastic squeegee, pressing from the center of the CD outwards (Fig. 4d). The sample reservoir was created by drilling a hole through the polycarbonate CD after transferring the channel layer. After modifying the channel surfaces, the reagents were deposited and lyophilized. The clear cover layer with air holes

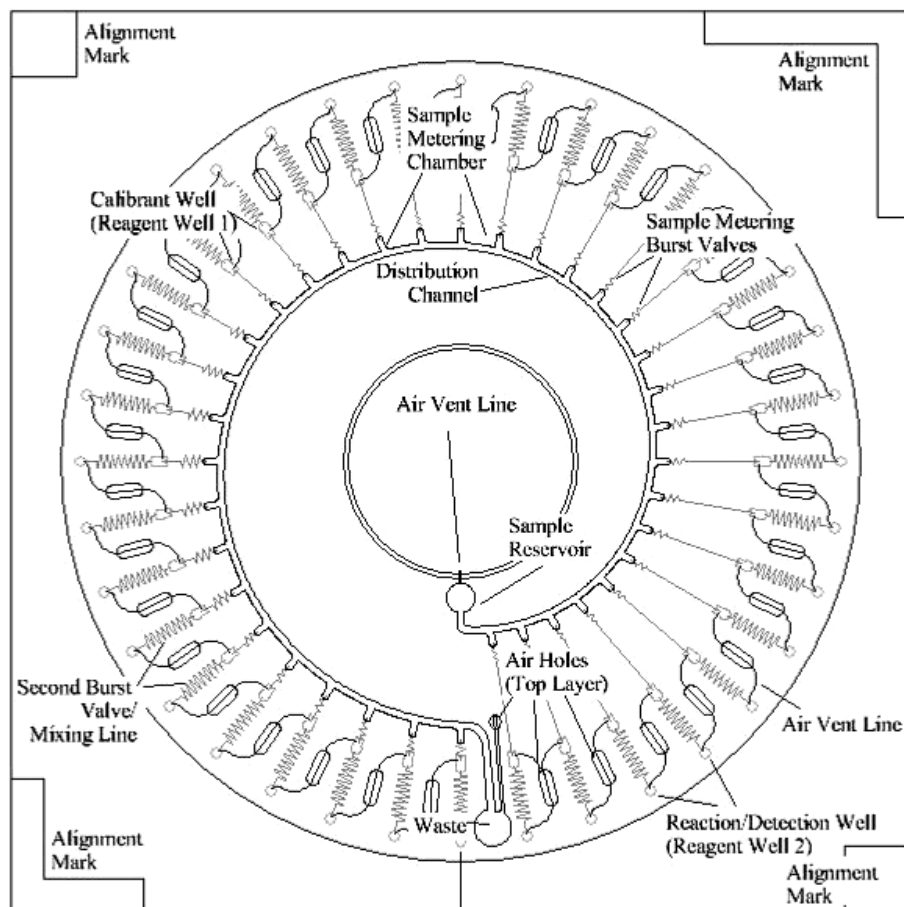


Figure 3: Layout of 36 sample metering chambers with separate reaction lines on the ChemCD

was then aligned and transferred to the CD using the same methods (Fig. 4a-d). Rotational alignment came from marks on the CD and the alignment jig. Alignment using the jig had $\pm 200 \mu\text{m}$ accuracy. The adhesive film cover allowed the channels to be sealed and enzymes to be packaged without exposing them to excessive heat or harsh chemicals.

2.1.2. Surface modification

The CD and vinyl films had to be modified to make hydrophobic valves for the sample metering chambers, and hydrophilic channels for easier sample delivery in the distribution channel. The CD channels and valves were made hydrophobic using Granger's wash-in waterproofing solution for synthetic materials (Granger USA, Everett, WA). The solution consists of fluorocarbons emulsified in water with a detergent and has been used by others to make super-hydrophobic surfaces in patterned SU-8¹⁵. After the channel layer was cut and transferred to the CDs, the covered CDs were then baked at 55°C for 30 minutes in a dry oven. (The Quantum 200 film can withstand temperature up to 85°C .) This first baking step served two purposes. First, since single slices were only about $30 \mu\text{m}$ at the top end of the slice and about $10 \mu\text{m}$ at the bottom end of the slice, flow in the slices was restricted and tended to clog easily. Heating the material shrunk the vinyl film, expanding the single slices to about $80 \mu\text{m}$ (top and bottom of the slice). This increased the flow and reduced clogging. Second, since the Granger's solution had to be cured above 54°C for optimal hydrophobicity and fluoropolymers alignment¹⁶. Pre-shrinking the channels prevented uncoated channel regions from being exposed during the final curing bake. After the first bake, the whole CD was placed in the Granger's wash-in solution, diluted $50\times$ with deionized water, for 30 minutes. After soaking, the CDs were rinsed gently in DI water and dried with an air nozzle. The CDs were then cured at 55°C for 30 minutes. After the final bake, the channels had expanded again but ranged from $60\text{--}150 \mu\text{m}$. The final contact angle on the polycarbonate CDs and vinyl films was $116\pm 2^\circ$.

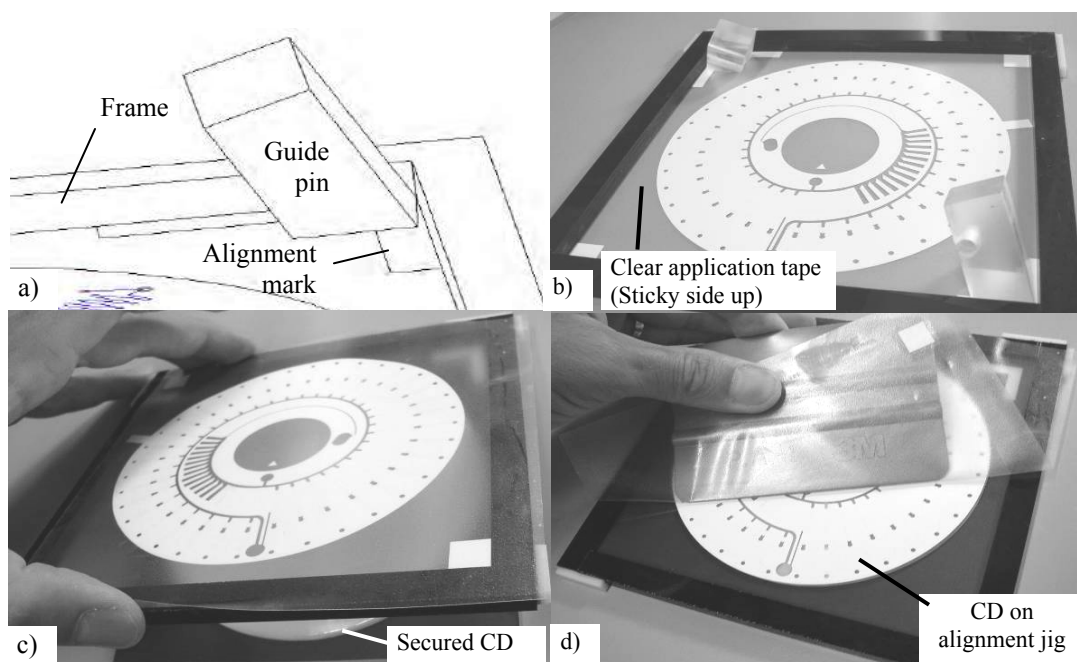


Figure 4: Alignment of channel and cover layers cut in adhesive films onto a polycarbonate CD.

A stamp molded in poly(dimethylsiloxane) (PDMS) was used to pattern bovine serum albumin (BSA) in the distribution channel and reagent wells to render them hydrophilic. The PDMS stamp was wetted on a filter paper soaked in 5 mg/ml of BSA and then pressed onto the CD. The PDMS stamp was made by casting a 10:1 mixture of PDMS oligomer and cross-linking agent (Sylgard 184, Dow Corning, Midland, MI)¹⁷ onto a mold machined in acrylic using conventional computerized numerically controlled (CNC) machining. Mold features were 1 mm thick and down to 1 mm in diameter. The BSA passivated the reagent well surfaces to protect the bioluminescent enzymes from adsorbing to the surface and denaturing. The contact angle of the BSA coated surfaces was 21 ± 2 degrees.

2.2. Deposition and lyophilization

A dispensing system using miniature solenoid valves (INKX0516350AA, The Lee Co.) capable of dispensing 40 to 500 nL ($\pm 5\%$) droplets was used to dispense the reagents. Each solenoid had 1.97" long stainless steel nozzles (O.05" OD, 0.031" ID) fit with 0.005" (± 0.0002 ") laser cut sapphire orifices (INZX0530450AA, The Lee Co.). Up to 24 μ L of enzyme reagents could be aspirated into each solenoid without contaminating the solenoid's active parts. A spike and hold driver circuit (IECX0501350AA, The Lee Co.) was used to open and hold the solenoids for extended periods of time when aspirating and cleaning the nozzles, without over heating the solenoid. The 24 V spike was set to 250 microseconds, the shortest spike width required to consistently open the solenoid. The holding voltage was set to 3.1 V, the lowest voltage required to hold the solenoid open. Pulse width and number of pulses were controlled by a National Instruments PCI 6601 counter card.

The valves were plumbed to a computer controlled syringe pump (0162573 PSD/2, Hamilton Co.) fitted with an eight port valve and a 500 μ L syringe. A LabVIEW program was used to communicate with the PSD/2 via the computer's serial COM port. The pulses from the PCI 6601 counter card were directed to one of six spike and hold driver circuits by a 8 channel multiplexer (DG408DJ, Analog Devices) which was controlled by TTL output signals from the PSD/2. The TTL outputs were controlled by serial commands from the LabVIEW program. Before dispensing, a three way T-valve opened the solenoid line to an air line that could be regulated at 5 PSI.

Six micro-solenoid dispensers were attached to a vertical stepper motor translation stage (VT-80-25-2SM, Phytron, Inc.). The dispensing platform was attached to an XY stepper motor translation stage (VT-80-150-2SM, Phytron, Inc.). The translation stages were controlled by a 4-axis motion control card (PCI-7334, National Instruments) via a

LabVIEW program. Each stepper motor was powered by a microstepper motor driver (Gecko G201A, ToolTech, Inc.) which resulted in a 0.5 μm step per pulse.

Enzyme dispensing was complete in about 25 seconds for each CD. Immediately after dispensing, the CDs were placed in the sample chamber of a VirTis Genesis 12 pilot plant lyophilizer, which was already cooled to -50°C . This allowed the reagents to freeze before evaporating, which would have denatured the enzymes. Primary lyophilization was performed at less than 100 mTorr with the condenser chamber cooled to -70°C for 48-72 hr. Secondary lyophilization was then performed for 12-24 hours after changing the sample chamber to 25°C at an average ramp rate of $\sim 3^{\circ}\text{C/hr}$. After lyophilization, the CDs were sealed with the cover layer as described above and stored in vacuum sealed aluminium coated nylon pouches.

2.3. Assays tested

The basic ATP bioluminescence assay was tested in the ChemCD to determine detection limits and the potential of onboard calibration. ATP was dispensed into the calibration wells (reagent well 1) in seven channels in different amounts and then allowed to air dry. During sample delivery, the ATP in each channel mixed with the 200 nL of metered sample of deionized (DI) water to act as a standard. Final concentrations of the sample mixed with the standards ranged from 0.001 μM to 100 μM in logarithmic increments, plus one blank. The standards then moved downstream to mix with the FFL reagents in the 2nd reagent wells. These 7 channels were repeated 5 times on the CD, leaving the 36th channel empty as a blank. The enzyme concentrations (200 μL each) dispensed in the reaction wells (reagent well 2) are listed in Table 1. The ATP test CDs also compared enzyme concentrations. 14 channels used 1 μM of firefly luciferase (FFL), another 14 used 2 μM , and another 7 used 5 μM FFL. The enzyme reagents were then dispensed into the reagent wells.

2nd Reagent Well (200 μL)	Assay Recipe (in μM)	Wells 1-14	Wells 15-28	Wells 29-35	Supplier
Platform Assay	Firefly Luciferase	1	2	5	Promega
	Luciferin	100	100	100	Biosynth
Buffer/excipients	Tricine pH 7.8		100,000		Sigma
	BSA		2 mg/mL		Sigma
	PEG (8kD)		2mg/mL		Sigma
	CoA		100		Fluka
	Mannitol		200,000		Pfanstiehl
	DTT		10,000		Fluka

Table 1: Assay concentrations for ATP tests.

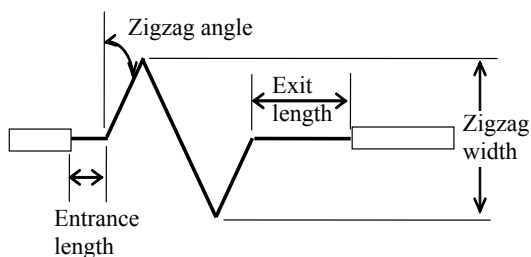


Figure 5: Example zigzag valve.

Assay Recipe (in μM)		Creatinine	Galactose	Glucose	Supplier
1st Reagent Well	ATP stock	200	200	1,000	Sigma
	Mg^{2+} (as SO_4)	5,000	5,000	50,000	Sigma
	Volume of ATP stock (nL)	200	40	200	
	Rehydrated ATP concentration	200	40	1,000	
2nd Reagent Well (200 nL dispensed)	Analyte specific enzyme				
	Creatine Deaminase	10			ICN
	N-methylhydantoinase	4			Roche
	NH_4^+	60			Sigma
	Galactokinase pH 8.5		1 U/mL		Sigma
	Glucokinase			10	Sigma
	Platform assay				
	Firefly Luciferase		1		Promega
	Luciferin		100		Biosynth
Buffer/excipients	Tricine pH 7.8		100,000		Sigma
	BSA		2 mg/mL		Sigma
	PEG (8kD)		2mg/mL		Sigma
	CoA		100		Fluka
	Mannitol		200,000		Pfanstiehl
	DTT		10,000		Fluka

Table 2: Assay concentrations for creatinine, galactose, and glucose tests.

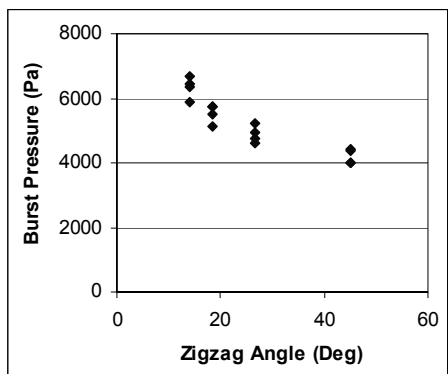


Figure 6: Burst pressure as a function of zigzag angle.

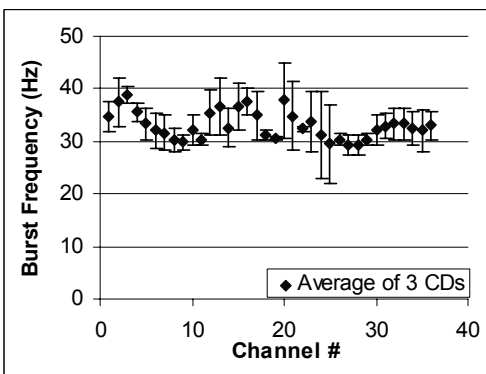


Figure 7: Average burst frequencies of the sample metering burst valves.

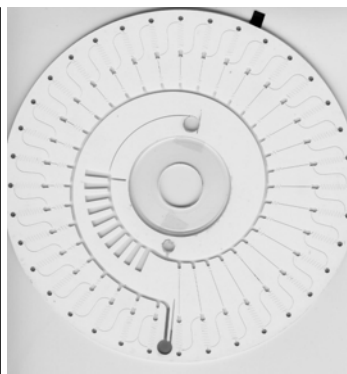


Figure 8: 200 μ L aliquots delivered to 36 reaction wells.

ChemCDs with assays for measuring creatinine, galactose, and glucose were also tested. The reagents and enzymes used are listed in Table 2. The ATP for the competition with the FFL reaction was placed in the first reagent well. The remaining reagents were dispensed and lyophilized in the 2nd reagent wells. Samples with varying concentrations of creatinine, galactose, and glucose were dispensed onto different CDs and the results were compared.

2.4. Sample delivery

The cover layer on the CD aligned over the channel layer, sealing the channels and one side of the hole that was drilled for the sample reservoir. The CDs were turned over to place 13 μ L samples in the other side of the hole and sealed with cellophane tape. The reservoir fed directly into the distribution channel.

Sample flow and observation was performed on a modified computer CD ROM for spinning the sample through the CD. The CD speed was controlled by sending an analog voltage from the data acquisition card to the voltage input line of the Hall effect motor driver chip on the CD ROM. The CD frequency was monitored by attaching an encoder wheel from the hub of the motor and reading the signal from another optical encoder. Flow visualization and indexing functionality was achieved by using a second optical encoder marking each rotation of the CD. An indexing tag was included on the CD channel layer when it was cut. As the indexing tag passed the encoder, it triggered a 50 μ s flash from a 12 V ultra bright LED array through a transistor switch. The flash was used to strobe the CD with each rotation, allowing the flow to be observed. The encoder signals were squared using a Schmitt trigger. Pulse functions, encoder indexing signals, and data acquisition was processed and controlled through two PCI data acquisition cards (PCI-6229 M and PCI-6036 E, National Instruments, Austin, TX). The PCI cards were installed in a desktop PC set to run with LabVIEW RTS as a real-time stand alone unit. The CD ROM and data acquisition was then controlled from a LabVIEW program on a laptop over the internet through an Ethernet line. The speed was controlled through a PID (Proportional Integral Derivative) feedback control loop to maintain program set speeds. The system was able to control speeds from 1 to 120 Hz with variability $\leq 1\%$.

The burst pressure of the zigzag valves were almost twice as high as would be expected based on the channel diameter ($D_h = 85 \mu\text{m}$)¹⁰. Therefore, burst pressure experiments were performed to determine which portion of the zigzag valve design components (Fig. 5) contributed to the increased burst pressures. No variability was seen in the burst pressure when the entrance and exit channels varied in length. The angle at which the zigzag turned did affect the burst pressure (Fig. 6). However, increasing the valve length by increasing the width of the zigzag or number of zigzag turns did not show in improvement in burst pressures. Thus, the improved burst pressure of a zigzagged burst valve is mainly due to the combination of capillary and hydrophobic valve effects at the zigzag turns like the vertical wall structured valves of Tiensuu *et al.*¹⁸.

The spiral distribution channel started at 25.5 mm and ended at 40 mm to ensure sample flowed at less than 20 Hz. The angle of the zigzag channels were changed for each sample metering burst valve to make them burst at about the same frequency (Fig. 7). To deliver a 13 μ L sample, the CD spin speed was ramped up from zero to 19 Hz over the course of 90 seconds to distribute the sample to all 36 sample metering chambers. The CD maintained 19 Hz for an additional 90 seconds to ensure the distribution channel was drained without prematurely bursting the sample metering valves. The CD

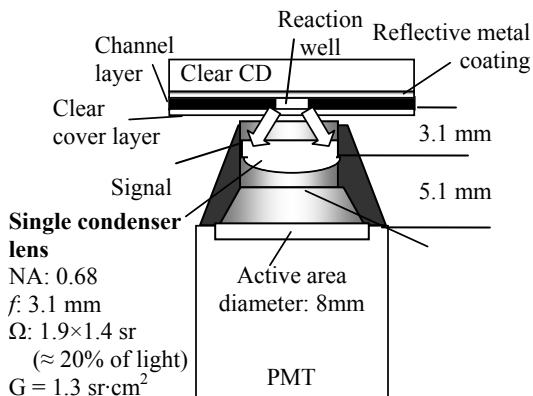


Figure 9: Optics for light collection.

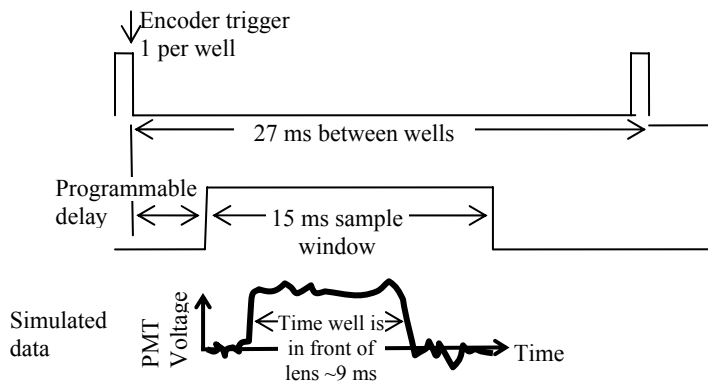


Figure 10: Sample acquisition timing diagram.

then spun ramped up to 90 Hz in 11 seconds and maintained that speed for an additional 15 seconds to ensure the 200 nL aliquots were delivered all the way to the reaction wells (Fig. 8). The CD then slowed down to 1 Hz within 10 seconds before acquiring the luminescent signal from each channel.

2.5. Light collection

To optimize the amount of light collected, the geometric extent G of the lens collection system was considered.

$$G = A_D \Omega \approx A_D \pi \left[1 - \cos \left(a \tan \left(\frac{D_L}{2f} \right) \right) \right] \quad (8)$$

where A_D is the area of the detector, f is the lens focal length, and D_L is the lens diameter, and Ω is the solid collection angle of the lens in steradian (sr)¹⁹. A Hamamatsu H5784 PMT (Hamamatsu Corp., Bridgewater, NJ) was chosen as the detector because of its size and built in amplifier (see Fig 9). The LightPath[®] aspheric lens (NT46-355, Edmund Optics, Barrington, NJ) was chosen for its short focus length (3.1 mm, with a working distance of 1.76 mm) relative to its clear aperture (5 mm), resulting in a collection angle of 1.4 sr (Fig 9). The small lens size and short focal length also allowed the reaction wells to be placed closer together without crosstalk between wells. The collection angle nearly doubles from the metalized coating on the CD. The best geometric extent possible with the chosen components and metalized CDs is 1.3 sr·cm². At the highest gain setting, the noise equivalent power of the PMT is 1.4×10^{-14} W (DC at 560 nm). Given the geometric extent determined above, the luminescent source must have a radiance greater than 1.1×10^{-14} W/sr/cm². (Radiance is a measure of the flux density per steradian²⁰).

2.6. Data collection

The PMT was attached to the optical carriage of the modified CD player. As the CD spun at 1 Hz, the rotation encoder triggered 150 samples at sampling rate of 100,000 Hz for each reaction well, after a specified delay (Fig. 10). Each 15 ms sample was integrated, indexed and sorted by well. The sensitivity of the PMT's anode was set to 14 V/nW for a 560 nm signal. The PMT has a built in current to voltage converter through a 1 MΩ resistor, converting the photocurrent by a factor of 1 V/μA. The integrated voltage samples were proportional to the number of photons generated during the sample collection period. The 1.6 mm diameter reaction wells were only in front of the collector lens for ~9 ms. The remaining integrated sample from the 15 ms window averaged out to the background noise of the system, which was 0.01 V. Data was recorded for about 200-300 seconds using the LabVIEW user interface described above.

3. DATA

3.1. ATP assay

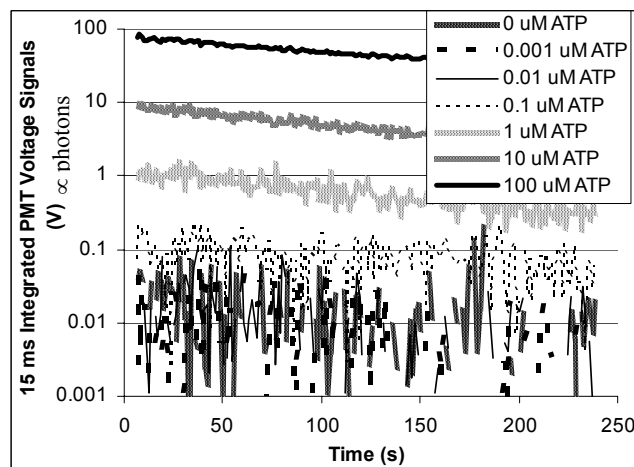


Figure 11: Kinetic data from multiple ATP standard channels from the 5 μ M FFL assay.

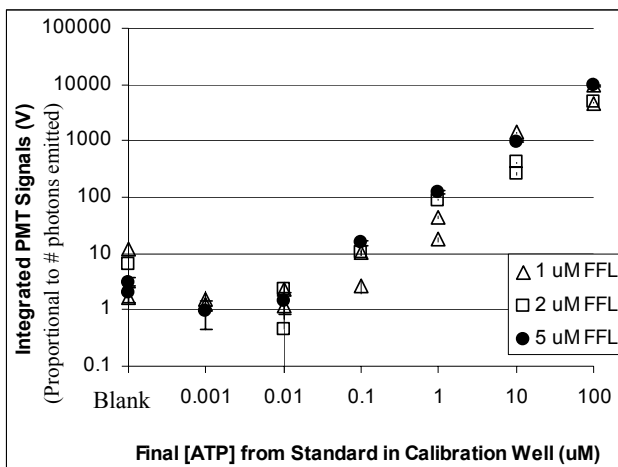


Figure 12: Calibration curves from the kinetic data of Fig. 11 integrated for 240 sec.

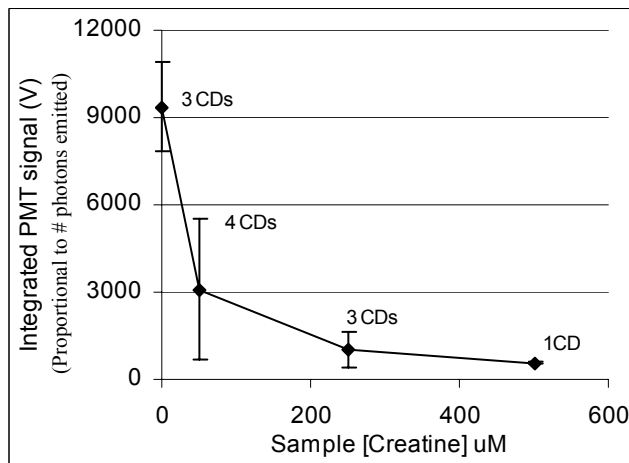


Figure 13: Standard curves from kinetic signals of the creatinine assays integrated 165 seconds.

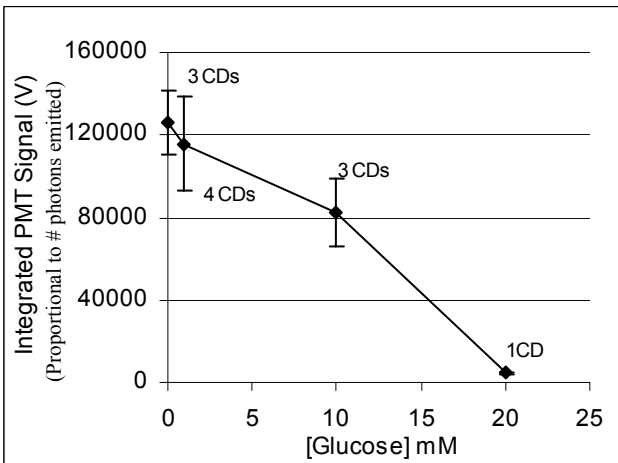


Figure 14: Standard curves from kinetic signals of the glucose assays integrated 220 seconds.

The logarithmic ATP standards packaged on the ChemCD mixed with the DI sample to produce logarithmic increases in intensity. The kinetic results for the 5 μ M FFL assay is plotted in Fig. 11. The resulting calibration curves for all the FFL assays tested are plotted in Fig. 12. The lowest measurable concentration was 0.1 μ M, which is a detection limit of 200 femtomoles. There was 9% error between wells of the same concentration. There appears to be little difference between concentrations of FFL used. The extra FFL at higher concentrations probably only functions as an excipient. There also appears to be a slight background luminescence for the blank sample, compared to the 0.001 and 0.01 μ M ATP samples. This could be due to background luminescence of the luciferin, or that at low ATP concentrations, the ATP binds to the FFL, holding it in a stable formation⁶.

3.2. Creatinine & glucose assays

The creatinine and glucose assays did not produce a 1:1 ratio of photons to the analyte concentration due to the competitive nature of the assays (Fig. 13&14). The intensity of the blank samples for the creatinine and glucose assay seemed to differ by a little over one order of magnitude, even though the ATP added to the glucose assay was only 5 \times that of the creatinine assay. The difference is probably due to better quantum efficiency, or better activity after lyophilization, of the creatinine deaminase compared to the glucose kinase, which means it consumes the ATP faster.

3.3. Galactose assay

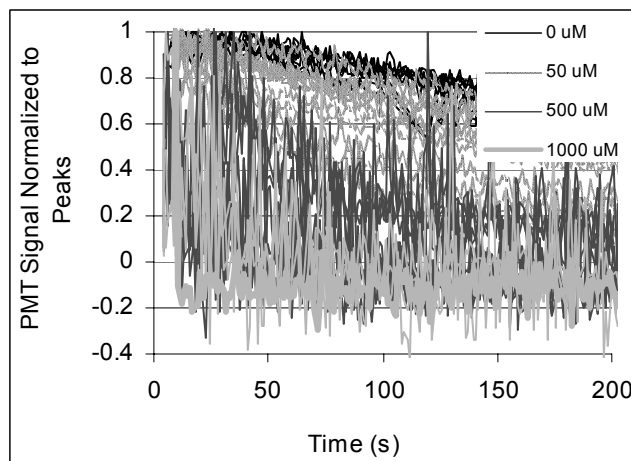


Figure 15: Kinetic data from galactose assays with varying sample concentrations. Each signal was normalized to its peak, therefore results are proportional to the change in $d\text{photon}/dt$.

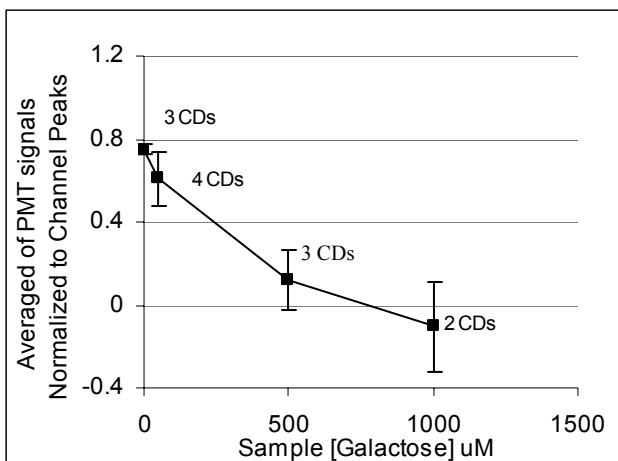


Figure 16: Standard curves after averaging the normalized kinetic data from Fig. 15. Data represents the average of the change in $d\text{photon}/dt$.

The galactose assay had to be calibrated by comparing the rate of change in intensity for each concentration. To do this, the PMT signals were normalized to the peak intensity of each channel (Fig 15). The normalized signals were then averaged to produce a standard curve (Fig 16).

4. RESULTS

Analyte	Smallest Measured Concentration	% Error Between CDs	Approximates Detection Limit (picomoles)
ATP	0.1 uM	20%	0.2
Creatinine	50 uM	78%	10
Galactose	50 uM	21%	10
Glucose	10 mM	20%	2,000

Table 3: Summarized results of the assays. The variability between channels on a single CD was 9%

The variability between channels on the ChemCD was 9%. The variability of the reagent dispenser accounts for 5% of that variability. Unfortunately, the variability between CDs was high as seen in Table 3. This high error is associated with not being able to capture the kinetic peaks of the competition signals. In order to compare the measurement between wells, the kinetic peaks are usually normalized, as was done with the galactose assay⁶. The CD ROM uses a Hall effect motor, so the CD could not stop immediately after the samples enter the reaction wells. Therefore, the signals peaks could not be measured right away. A stepper or servo motor with position control would work better to control the spin speed. It would hold each well in a stationary position directly above the lens for each data point measured.

5. CONCLUSIONS

The ChemCD was capable of distributing 200 nL sample aliquots to 36 channels, each with a different set of reagents. Although only a few assays were tested on the ChemCD, it has potential for measuring a variety of analytes from small sample volumes. The ChemCD can be designed to incorporate specific assays to test multiple diagnostic panels. Sequential mixing channels could be designed for a variety of assays, including immunoassays. Different microfluidic designs can easily be tested using xurography to build the prototypes. The optical system can be configured for fluorescent and absorbance assays by including the appropriate light sources and patterning clear sections on the CD.

Standards can be incorporated on the CD to perform some onboard calibration. Plasma separation from whole blood can also be incorporated into the design to make it even more practical for use at the point-of-care. The small sample volumes required means the blood can be acquired from small pin pricks, which improves patient comfort and makes testing easier. The ChemCD makes it possible to automatically perform sample preparation and measurements for multiple analytes and can easily be used for many point-of-care applications.

ACKNOWLEDGMENTS

This work was supported by the NIH RFP#PAR01-057, Project#1R21RR17329, Technology Development for Biomedical Applications Grant.

REFERENCES

1. J. V. Zoval and M. J. Madou, "Centrifuge-based fluidic platforms," *Proceedings of the IEEE*, **92**, 140-153, 2004.
2. M. Groves, "Point-of-care testing," *IVD Technology*, **April**, 2005.
3. U. Wendel and U. Langenbeck, "Towards self-monitoring and self-treatment in phenylketonuria--a way to better diet compliance," *Eur J Pediatr*, **155 Suppl 1**, S105-107, 1996.
4. S. Segal and G. Berry, "Disorders of galactose metabolism," in *The metabolic and molecular bases of inherited disease*, vol. 1, C. Scriver, Ed. 967-1000 McGraw-Hill, New York. 1995.
5. S. Brodin and G. Wettermark, *Bioluminescence analysis*. VCH, 1992.
6. R. H. Davies, "Luminescent assays for the assessment of metabolism and renal function: Towards a multianalyte biosensor," Ph.D. Dissertation. Department of Bioengineering, University of Utah, Salt Lake City, Utah, 2005.
7. R. H. Davies, D. A. Bartholomeusz, and J. D. Andrade, "Personal sensors for the diagnosis and management of metabolic disorders," *IEEE Engineering in Medicine and Biology Magazine*, **22**, 32-42, 2003.
8. J. D. Andrade, D. A. Bartholomeusz, R. H. Davies, X. Yang, and J. Janatova, "Multi-analyte bioluminescence-based disposable chemchips for home-based application," *Photonics West*, J. Fujimoto and R. R. Anderson, BIOS 2006, San Jose, CA, 2006.
9. N. Mizoguchi, H. Ono, T. Eguchi, and N. Sakura, "Galactose metabolites in blood from neonates with and without hypergalactosaemia detected by mass screening," *Eur J Pediatr*, **159**, 851-853., 2000.
10. D. C. Duffy, H. L. Gillis, J. Lin, N. F. Sheppard, Jr., and G. J. Kellogg, "Microfabricated centrifugal microfluidic systems: Characterization and multiple enzymatic assays," *Analytical Chemistry*, **71**, 4669-4678, 1999.
11. M. J. Madou, Y. Lu, S. Lai, J. Lee, and S. Daunert, "A centrifugal microfluidic platform - a comparison," *Micro Total Analysis Systems*, 565-570, The Netherlands, 2000.
12. J. A. Clements, "Sixth bowditch lecture: Surface phenomena in relation to pulmonary function," *The Physiologist*, **5**, 11-28, 1962.
13. J. D. Andrade and V. Hlady, "Plasma protein adsorption: The big twelve," *Ann N Y Acad Sci*, **516**, 1987.
14. D. A. Bartholomeusz, R. W. Boutté, and J. D. Andrade, "Xurography: Rapid prototyping of micro-structures using a cutting plotter," *IEEE Journal of Microelectromechanical Systems*, **14**, 1364-1374, 2005.
15. N. J. Shirtcliffe, S. Aqil, C. Evans, G. McHale, M. I. Newton, C. C. Perry, and P. Roach, "The use of high aspect ratio photoresist (su-8) for super-hydrophobic pattern prototyping," *Journal of Micromechanics and Microengineering*, **14**, 1384, 2004.
16. Personal communication with C. Mork, Axis Outdoor, 2005.
17. D. C. Duffy, J. C. McDonald, O. J. A. Schueller, and G. M. Whitesides, "Rapid prototyping of microfluidic systems in poly(dimethylsiloxane)," *Analytical Chemistry*, **70**, 4974-4984, 1998.
18. A.-L. Tiensuu, O. Ohmann, L. Lundblad, and O. Larsson, "Hydrophobic valves by ink-jet printing on plastic cds with integrated microfluidics," *Micro Total Analysis Systems*, 575-578, The Netherlands, 2000.
19. R. McCluney, *Introduction to radiometry and photometry*. 424, Artech House Publishers, 1994.
20. A. Ryer, "Light measurement handbook." Newburyport, MA: International Light Inc., 1998.

Handwritten:
N. G. Cal
3-16-06

Advanced Biomedical and Clinical Diagnostic Systems IV

Gerald E. Cohn
Warren S. Grundfest
David A. Benaron
Tuan Vo-Dinh
Chairs/Editors

22-24 January 2006
San Jose, California, USA

Sponsored and Published by
SPIE—The International Society for Optical Engineering

Volume 6080



The International Society
for Optical Engineering

SPIE is an international technical society dedicated to advancing engineering and scientific applications of optical, photonic, imaging, electronic, and optoelectronic technologies.